California forest die-off linked to multi-year deep soil drying in 2012-2015 drought

M. L. Goulden [1]*, R.C. Bales[2]

[1]Department of Earth System Science, University of California, Irvine, CA 92697-3100, USA.
[2]School of Engineering, and [3]Sierra Nevada Research Institute, University of California, Merced, CA 95343, USA.
*Corresponding author: mgoulden@uci.edu

Widespread episodes of recent forest die-off have been tied to the occurrence of anomalously warm droughts, though the underlying mechanisms remain inadequately understood. California's 2012-2015 drought, with exceptionally low precipitation and warmth and widespread conifer death, provides an opportunity to explore the chain of events leading to forest die-off. Here we present the spatial and temporal patterns of die-off and moisture deficit during California's drought based on field and remote-sensing observations. We found that die-off was closely tied to multi-year deep-rooting-zone drying, and that this relationship provides a framework to diagnose and predict mortality. Marked tree death in an intensively studied Sierra Nevada forest followed a four-year moisture overdraft, with cumulative 2012-2015 evapotranspiration exceeding precipitation by ~1500 mm and subsurface moisture exhaustion to 5-15 m depth. Observations across the entire Sierra Nevada further linked tree death to deep drying, with die-off and moisture overdraft covarying across latitude and elevation. Unusually dense vegetation and warm temperatures accelerated southern Sierran evapotranspiration in 2012-2015, intensifying overdraft and compounding die-off by an estimated 55%. Climate change is expected to further amplify evapotranspiration and moisture overdraft during drought, potentially increasing Sierran tree death during drought by ~15 to 20% per °C.

Growing evidence indicates recent episodes of forest die-off have been intensified by the interacting effect of drought plus anomalous warmth[1-6], though the mechanisms remain uncertain and a more quantitative understanding is needed for diagnosis and projection[7-9]. We combined in-situ and remote sensing observations to explore the links between drought, warmth, vegetation density and forest dieback in California's mountains (Figure S1).

The 2012-2015 drought spanned California, and was especially severe in the southern Sierra Nevada[10-13]. Each year had below average precipitation (*P*; Fig. 1a) and the four-year period was the Sierra's driest in the last century. Each year was warmer than average, and 2014 and 2015 were among the warmest in the Sierran instrumental record. This warmth intensified the lack of precipitation[12], and the drought is considered the most extreme in the last 100 to 1000 years[10].

Marked tree mortality occurred in California's mountains, with many stands experiencing a nearly complete loss of mature conifers. Mortality was greatest among pines, often in association with bark-beetle outbreaks. The US Forest Service (USFS) Aerial Detection Survey (ADS)[14], which uses spotters to inventory tree death from aircraft, found rapidly accelerating mortality in 2015 and 2016, especially in the southern Sierra (Fig. 1b). The late dry-season Landsat Normalized Difference Moisture Index (*NDMI*[15,16,17]) provides a second approach to mapping dieback. The spatial patterns of *NDMI* decline were correlated with the ADS mortality across the full Sierra Nevada (Fig. S2a, S3). *NDMI* detects the density of hydrated leaves, and the *NDMI* decline from 2014 to 2016 indicates marked evergreen canopy loss (Fig. 1b).

Both the ADS and late dry-season *NDMI* indicated mortality was greatest in the lower reaches of conifer forest. Mortality began at lower elevations in 2014 and accelerated and rose with time, becoming widespread throughout the lower conifer forest by 2015 (Fig. 1c). Previous aircraft and satellite surveys reported similar patterns of dieback across space and time[11,18,19].

Sequence of events leading to forest die-off

Drought and mortality were severe at the Southern Sierra Critical Zone Observatory (SSCZO)[13]. Field observations at the SSCZO began before and continued through the drought, providing a direct record of the sequence of events leading to dieback.

The SSCZO includes four focal sites along an elevation and climate gradient[20] (37.11° to 37.03°N, -119.73° to -118.99°W; Fig. S1). Temperature decreases and *P* increases with elevation, while vegetation shifts from oak savanna at 405 m, to conifer forest at 1160 and 2015 m, to subalpine forest at 2700 m. Vegetation density and Leaf Area Index (*LAI*) are greatest in mid-elevation conifer forest, and decline with precipitation at lower elevation and colder temperatures higher up[21]. A post-drought resurvey showed mortality was greatest at 1160 m (79% basal area loss in 2016 relative to 2010), and less-severe at 2015 m (21% loss), 405 m (2% loss) and 2700 m (6% loss). Late dry-season *NDMI* declined markedly from 2014 to 2016 at 1160 m, and to a lesser extent at 2015 m (Fig. 2a). This agrees with anecdotal observations at 1160 m of peak mortality among pines in July and August 2015 coincident with a drought-driven bark-beetle outbreak, and later among other conifers at 1160 m and all conifers at 2015 m.

Eddy-covariance measurements of gross CO_2 uptake at 1160 m[20], which provides a measure of whole-forest photosynthesis, showed progressively intense and longer-lasting dry-season shutdowns (Fig. 2b, S4). CO_2 uptake continued nearly year-round during the first drought year, with a modest shutdown in summer. The dry-season

shutdowns became longer and deeper over the drought and CO_2 uptake was restricted to the ~six-month winter and spring wet season during later years.

A location's water balance may be defined as $P - ET = \Box S + Q$, where ET is evapotranspiration, $\Box S$ is the change in root-accessible moisture storage and Q is the net subsurface and overland flow[13]. $\Box S$ is less important during moisture excess, and P-ET approximates Q. Conversely, Q is reduced during drought, and a sustained P-ET overdraft implies subsurface drying. The cumulative P-ET deficit at 1160 m peaked at -1500 mm in summer 2015, implying a large net withdrawal of moisture from soil and weathered rock (Fig. 2c). The four-year water deficit at the 2015 m site was less severe, with a 120 mm P-ET overdraft and a cumulative Q of 330 mm[13] implying a $\Box S$ of -450 mm.

Both coring and geophysical observations have shown that Sierra Nevada regolith is porous and potentially root-accessible to a depth of 2 to 35 m[22,23]. The volumetric water-storage capacity at 1160 m averages 0.2 cm^3 cm^{-3} in the upper 5 m and decreases to 0.05 cm^3 cm^{-3} at greater depth[22], implying an integrated water storage capacity to 10 m depth of 1250 mm. In-situ measurements throughout the upper 4.5 m of regolith at the 1160-m site confirmed uniform drying to 0.05 cm^3 cm^{-3} or -1.5 MPa during the drought, with rewetting to 0.25 cm^3 cm^{-3} in 2017[13,23]. In-situ measurements to 10-m depth at 2015 m showed less-severe drying to 0.10 cm^3 cm^{-3} in 2015 and subsequent rewetting. The direct observations of subsurface moisture confirm the P-ET analyses and point to an exhaustion of subsurface moisture to a depth of at least 5 m, and probably 10 to 15 m, at 1160 m, with similarly deep but less-complete drying at 2015 m.

The more-extreme moisture overdraft at 1160 m was mirrored by greater die-off at lower elevation (Fig. 2a). The ET at both 1160 m and 2015 m increased strongly with temperature, with similar rates at both sites for a given temperature (Fig. S5). The mean temperature at 1160 m was 7°C warmer than at 2015 m, implying that temperature was an important cause of the greater P-ET overdraft and more-severe drying at lower elevation.

Semi-arid trees are deeply rooted, and belowground moisture buffers multi-year dry periods[13,22,24,25]: the 2012-2015 drought exceeded this safety margin. The main proximate cause of conifer mortality at 1160 m was a bark-beetle outbreak in August 2015, and the ultimate cause appears to be exhaustion of root-accessible moisture (see also[8,26,27]). The cumulative P-ET overdraft at 1160 m followed a decay trajectory, with a rapid initial decline to a new equilibrium of -1500 mm (Fig. 2c). We divided the sequence of events leading to die-off into two phases: a *drying phase* from June 2011 to August 2013 at 1160 m, and a *stress phase* from August 2013 to August 2015. The *drying phase* was marked by the net withdrawal of deep moisture to support continued high rates of CO_2 uptake and ET. The *stress phase* was marked by subsurface moisture exhaustion, reduced CO_2 uptake and ET with stomatal closure, and progressive leaf and canopy dieback. The *drying phase* depleted the plant accessible moisture reservoir, and the

stress phase marked the deterioration of vegetation health, increasing pathogen attack and ultimate die-off.

Spatial tie between die-off and moisture overdraft

We combined *NDMI*, interpolated estimates of precipitation[28], and satellite estimates of ET based on the Normalized Difference Vegetation Index *(NDVI;* Fig. S6) to investigate the relationship between dieback and P-ET across the entire Sierra Nevada (Fig. S1). The resulting spatial patterns of P-ET were qualitatively and quantitatively similar to independent measures of large-scale water balance. The inter-annual and spatial patterns of P-ET were well correlated with the river flows (Q) observed for large Sierran river basins[13,20,21,24]. Analyses of 2012-2015 GPS records showed an anomalous ~20 mm uplift in the Sierra Nevada with net drying and mass loss[29]. This uplift was greatest in the southern Sierra and corresponded to a regional net loss of ~1000 mm of water ($\Box S$), which is similar to the regional P-ET overdraft we calculated.

Cumulative moisture depletion and dieback were well correlated across the Sierra Nevada (Fig. 3, S2bc), with an inflection at a cumulative P-ET near zero. Late-drought dieback was minor at locations where P exceeded ET, and increased with a deepening overdraft. Gridded estimates of evergreen dieback ($\Box NDMI$) and P-ET overdraft showed higher values in the southern Sierra (35.7-37.7° N) and below 2300-m elevation. The latitudinal pattern of P-ET was tied to the latitudinal pattern of precipitation shortfall, which was greatest in the southern Sierra (Fig. S7a). The altitudinal pattern of P-ET was linked to ET (Fig. S8), which was greatest below 2300 m with denser canopies[13,20,21] and warmer conditions (Fig. S5).

Denser canopies were found on northern aspects relative to southern aspects in association with contrasting thermal loads and evaporative demand[21] (Fig. S9). The differing canopy densities acted to offset the hydrologic advantages of more mesic positions in the physical landscape, and led to a comparatively uniform distribution of canopy dieback with aspect.

The Palmer Drought Severity Index (*PDSI*), Standardized Precipitation-Evapotranspiration Index (*SPEI*) and Standardized Precipitation Index (*SPI*) failed to fully capture the observed dieback (Fig. S2, S7, S8). All three indices focus on atmospheric conditions and do not consider vegetation or soil properties that control ET such as canopy density and rooting depth, leading to weaker correlations with dieback, especially with elevation.

Comparison of 2012-2015 and 1987-1992 droughts

California has a long history of episodic drought and forest die-off[4]. The 1987 to 1992 period was also quite dry (Fig. 1a), though tree death in the southern Sierra appears to have been much less extreme[30]. The southern Sierra *NDMI* during 1987-1992 did not indicate a large evergreen canopy dieback, and the P-ET overdraft in 1987-1992 was much less extreme than in 2012-2015 (Fig. 4a).

The severity of P-ET overdraft in 2012-2015 compared to 1987-1992 reflected a greater P shortfall plus the effects

of warmth and antecedent canopy expansion on ET (Fig. 1a, 4b, S10). The P shortfall in 2012-2015 was greater than in 1987-1992, and air temperatures were 1.2°C warmer[12]. Moreover, the ET estimated solely from vegetation density ($ET_{just\ NDVI}$) was higher in 2012-2015 than 1987-1992 as a result of antecedent canopy expansion around 1994-1996 and 2009-2012 (Fig. S10, e.g., structural overshoot[9]). These three factors increased the drought's severity (Fig. 4b), with warmth amplifying the 2012-2015 P-ET overdraft by ~45% ($ET_{just\ T}$) relative to the long-term mean (ET_{mean}), and antecedent canopy expansion amplifying it by another ~45% ($ET_{just\ NDVI}$). The combination of warming and structural overshoot increased P-ET by ~90% ($ET_{T\&NDVI}$), which corresponds to a ~55% increase in tree death (Fig. S2b).

Implications

Canopy loss during the warm drought was greatest in lower-elevation forest, a pattern that mirrors previous observations of enhanced trees death in the lower reaches of species' distribution[4,31]. The enhanced tree vulnerability at lower elevation contrasts with predictions of enhanced hydrologic vulnerability at higher elevation[21]. A tradeoff between ecological and hydrologic vulnerability appears likely, with warming leading to greater episodic forest die-off at lower elevations and reduced runoff generation at higher elevation.

Our analysis provides a quantitative framework that links tree die-off to cumulative deep-soil drying, and that may be used to diagnose and predict die-off based on the underlying physical and biological properties and processes (Fig. S11). Key controls on die-off include the rate of cumulative P-ET decline (e.g., the slope of P-ET decline during the *drying phase* (6/2011 to 8/2013 at 1160 m); Fig. 2c), the plant-accessible water-storage capacity as determined by rooting depth, porosity and water flow[22] (e.g., the P-ET overdraft at moisture exhaustion), and the rate that biotic stresses develop after subsurface drying (e.g., the timing of vegetation decline and pathogen buildup during the *stress phase* (8/2013 to 8/2015)). Each of these factors is potentially sensitive to climate change.

Climate change that intensifies moisture overdraft during drought, including warming[32] that accelerates ET, or increased precipitation volatility[33,34] that promotes structural overshoot[9], is expected to amplify episodic die-off (Fig. S11). We estimate additional warming on top of a 2012-2015 precipitation shortfall would increase the P-ET overdraft by ~20 to 30% °C^{-1} (Fig. S5) and increase tree death by ~15 to 20% °C^{-1} (Fig. S2b).

The effect of previous canopy expansion on P-ET underscores the role of structural overshoot in amplifying the impact of climate change. Increases in canopy density often occurred when warm years followed wet ones (1996, 2000 and 2012 in Fig. S10). The canopy expansion in 2012 coincided with the first year of drought; 2012 was warmer than average and growth may have been supported by water or carbohydrate carryover from wet years in 2010 and 2011. The resulting dense canopy accelerated ET and intensified the subsequent P-ET overdraft. Much of the forest at ~1000-2500 m elevation is co-limited by water availability and winter cold[21,35], and the expansion of canopy during wetter and warmer periods is consistent with plants capturing space and resources during favorable periods. This vegetation maintains cover during average years, but the aggregate LAI exceeds the site carrying capacity during the least favorable periods[9,36]. A similar phenomenon occurs spatially, with northern aspects experiencing higher die-off despite more mesic conditions, presumably as a result of previous canopy expansion (Fig. S9).

Projections of future precipitation are uncertain, with marked variation between models and ensemble members[37], but a general agreement that P variability in many semiarid regions, including the western US, will intensify[33,34]. This raises the possibility that more extreme wet and warm years will accelerate episodic canopy expansion, with implications for subsequent tree death during warm droughts, and a range of positive and negative ecosystem services[27,38]

References

1 Breshears, D. D. *et al.* Regional vegetation die-off in response to global-change-type drought. *Proceedings of the National Academy of Sciences of the United States of America* **102**, 15144-15148, doi:10.1073/pnas.0505734102 (2005).

2 van Mantgem, P. J. *et al.* Widespread Increase of Tree Mortality Rates in the Western United States. *Science* **323**, 521-524, doi:10.1126/science.1165000 (2009).

3 Allen, C. D. *et al.* A global overview of drought and heat-induced tree mortality reveals emerging climate change risks for forests. *Forest Ecology and Management* **259**, 660-684, doi:10.1016/j.foreco.2009.09.001 (2010).

4 Fellows, A. W. & Goulden, M. L. Rapid vegetation redistribution in Southern California during the early 2000s drought. *Journal of Geophysical Research-Biogeosciences* **117**, doi:10.1029/2012jg002044 (2012).

5 Williams, A. P. *et al.* Temperature as a potent driver of regional forest drought stress and tree mortality. *Nature Climate Change* **3**, 292-297, doi:10.1038/nclimate1693 (2013).

6 Allen, C. D., Breshears, D. D. & McDowell, N. G. On underestimation of global vulnerability to tree mortality and forest die-off from hotter drought in the Anthropocene. *Ecosphere* **6**, 55, doi:10.1890/es15-00203.1 (2015).

7 McDowell, N. *et al.* Mechanisms of plant survival and mortality during drought: why do some plants survive while others succumb to drought? *New Phytologist* **178**, 719-739, doi:10.1111/j.1469-8137.2008.02436.x (2008).

8 McDowell, N. G., Ryan, M. G., Zeppel, M. J. B. & Tissue, D. T. Improving our knowledge of drought-induced forest mortality through experiments, observations, and modeling. *New Phytologist* **200**, 289-293, doi:10.1111/nph.12502 (2013).

9 Jump, A. S. *et al.* Structural overshoot of tree growth with climate variability and the global spectrum of drought-induced forest dieback. *Global Change Biology* **23**, 3742-3757, doi:10.1111/gcb.13636 (2017).

10 Griffin, D. & Anchukaitis, K. J. How unusual is the 2012-2014 California drought? *Geophysical Research Letters* **41**, 9017-9023, doi:10.1002/2014gl062433 (2014).

11 Asner, G. P. *et al.* Progressive forest canopy water loss during the 2012-2015 California drought. *Proceedings of the National Academy of Sciences of the United States of America* **113**, E249-E255, doi:10.1073/pnas.1523397113 (2016).

12 Williams, A. P. *et al.* Contribution of anthropogenic warming to California drought during 2012-2014. *Geophysical Research Letters* **42**, 6819-6828, doi:10.1002/2015gl064924 (2015).

13 Bales, R. C. *et al.* Mechanisms controlling the impact of multi-year drought on mountain hydrology. *Scientific Reports* **8**, 8, doi:10.1038/s41598-017-19007-0 (2018).

14 Coleman, T. W. *et al.* Accuracy of aerial detection surveys for mapping insect and disease disturbances in the United States. *Forest Ecology and Management* **430**, 321-336, doi:10.1016/j.foreco.2018.08.020 (2018).

15 Hardisky, M. A., Klemas, V. & Smart, R. M. The influence of soil-salinity, growth form, and leaf moisture on the spectral radiance of Spartina-alterniflora canopies. *Photogrammetric Engineering and Remote Sensing* **49**, 77-83 (1983).

16 Yilmaz, M. T., Hunt, E. R. & Jackson, T. J. Remote sensing of vegetation water content from equivalent water thickness using satellite imagery. *Remote Sensing of Environment* **112**, 2514-2522, doi:10.1016/j.rse.2007.11.014 (2008).

17 Goodwin, N. R. *et al.* Estimation of insect infestation dynamics using a temporal sequence of Landsat data. *Remote Sensing of Environment* **112**, 3680-3689, doi:10.1016/j.rse.2008.05.005 (2008).

18 Byer, S. & Jin, Y. F. Detecting Drought-Induced Tree Mortality in Sierra Nevada Forests with Time Series of Satellite Data. *Remote Sensing* **9**, 23, doi:10.3390/rs9090929 (2017).

19 Paz-Kagan, T. *et al.* What mediates tree mortality during drought in the southern Sierra Nevada? *Ecological Applications* **27**, 2443-2457, doi:10.1002/eap.1620 (2017).

20 Goulden, M. L. *et al.* Evapotranspiration along an elevation gradient in California's Sierra Nevada. *Journal of Geophysical Research-Biogeosciences* **117**, 13, doi:10.1029/2012jg002027 (2012).

21 Goulden, M. L. & Bales, R. C. Mountain runoff vulnerability to increased evapotranspiration with vegetation expansion. *Proceedings of the National Academy of Sciences of the United States of America* **111**, 14071-14075, doi:10.1073/pnas.1319316111 (2014).

22 Klos, P. Z. *et al.* Subsurface plant-accessible water in mountain ecosystems with a Mediterranean climate. *Wiley Interdisciplinary Reviews-Water* **5**, 14, doi:10.1002/wat2.1277 (2018).

23 O'Geen, A. *et al.* Southern Sierra Critical Zone Observatory and Kings River Experimental Watersheds: A Synthesis of Measurements, New Insights, and Future Directions. *Vadose Zone Journal* **17**, 18, doi:10.2136/vzj2018.04.0081 (2018).

24 Fellows, A. W. & Goulden, M. L. Mapping and understanding dry season soil water drawdown by California montane vegetation. *Ecohydrology* **10**, doi:10.1002/eco.1772 (2017).

25 Schenk, H. J. & Jackson, R. B. Rooting depths, lateral root spreads and below-ground/above-ground allometries of plants in water-limited ecosystems. *Journal of Ecology* **90**, 480-494, doi:10.1046/j.1365-2745.2002.00682.x (2002).

26 Anderegg, W. R. L. *et al.* Tree mortality from drought, insects, and their interactions in a changing climate. *New Phytologist* **208**, 674-683, doi:10.1111/nph.13477 (2015).

27 Franklin, J. F., Shugart, H. H. & Harmon, M. E. Tree death as an ecological process. *Bioscience* **37**, 550-556, doi:10.2307/1310665 (1987).

28 Daly, C. *et al.* Physiographically sensitive mapping of climatological temperature and precipitation across the conterminous United States. *International Journal of Climatology* **28**, 2031-2064, doi:10.1002/joc.1688 (2008).

29 Argus, D. F. *et al.* Sustained Water Loss in California's Mountain Ranges During Severe Drought From 2012 to 2015 Inferred From GPS. *Journal of Geophysical Research-Solid Earth* **122**, 10559-10585, doi:10.1002/2017jb014424 (2017).

30 Ferrell, G. T. *The influence of insect pests and pathogens on Sierra forests*. In: Sierra Nevada Ecosystem Project: Final report to Congress, vol. II. University of California, Centers for Water and Wildlands Resources, Davis, California; 1177-1192 (1996).

31 Kelly, A. & Goulden, M. Rapid shifts in plant distribution with recent climate change. *Proceedings of the National Academy of Sciences of the United States of America* **105**, 11823-11826, doi:10.1073/pnas.0802891105 (2008).

32 Pierce, D. W. *et al.* Probabilistic estimates of future changes in California temperature and precipitation using statistical and dynamical downscaling. *Climate Dynamics* **40**, 839-856, doi:10.1007/s00382-012-1337-9 (2013).

33 Swain, D. L., Langenbrunner, B., Neelin, J. D. & Hall, A. Increasing precipitation volatility in twenty-first-century California. *Nature Climate Change* **8**, 427-433, doi:10.1038/s41558-018-0140-y (2018).

34 Berg, N. & Hall, A. Increased Interannual Precipitation Extremes over California under Climate Change. *Journal of Climate* **28**, 6324-6334, doi:10.1175/jcli-d-14-00624.1 (2015).

35 Trujillo, E., Molotch, N. P., Goulden, M. L., Kelly, A. E. & Bales, R. C. Elevation-dependent influence of snow accumulation on forest greening. *Nature Geoscience* **5**, 705-709, doi:10.1038/ngeo1571 (2012).

36 Wilmers, C. C., Post, E. & Hastings, A. A perfect storm: The combined effects on population fluctuations of autocorrelated environmental noise, age structure, and density dependence. *American Naturalist* **169**, 673-683, doi:10.1086/513484 (2007).

37 Deser, C., Phillips, A. S., Alexander, M. A. & Smoliak, B. V. Projecting North American Climate over the Next 50 Years: Uncertainty due to Internal Variability. *Journal of Climate* **27**, 2271-2296, doi:10.1175/jcli-d-13-00451.1 (2014).

38 Thom, D. & Seidl, R. Natural disturbance impacts on ecosystem services and biodiversity in temperate and boreal forests. *Biological Reviews* **91**, 760-781, doi:10.1111/brv.12193 (2016).

Acknowledgements

Agriculture (USDA; 2018-67004-27405), and the University of California Laboratory Fees Research Program. The eddy-covariance sites were located at the San Joaquin Experimental Range, the King River Experimental Watershed, and on the Sierra National Forest in cooperation with the USFS.

Author contributions
M.L.G. and R.C.B. designed research; M.L.G. performed research; M.L.G. analyzed data; and M.L.G. and R.C.B. wrote the paper.
**Competing interests**
The authors declare no competing interests.
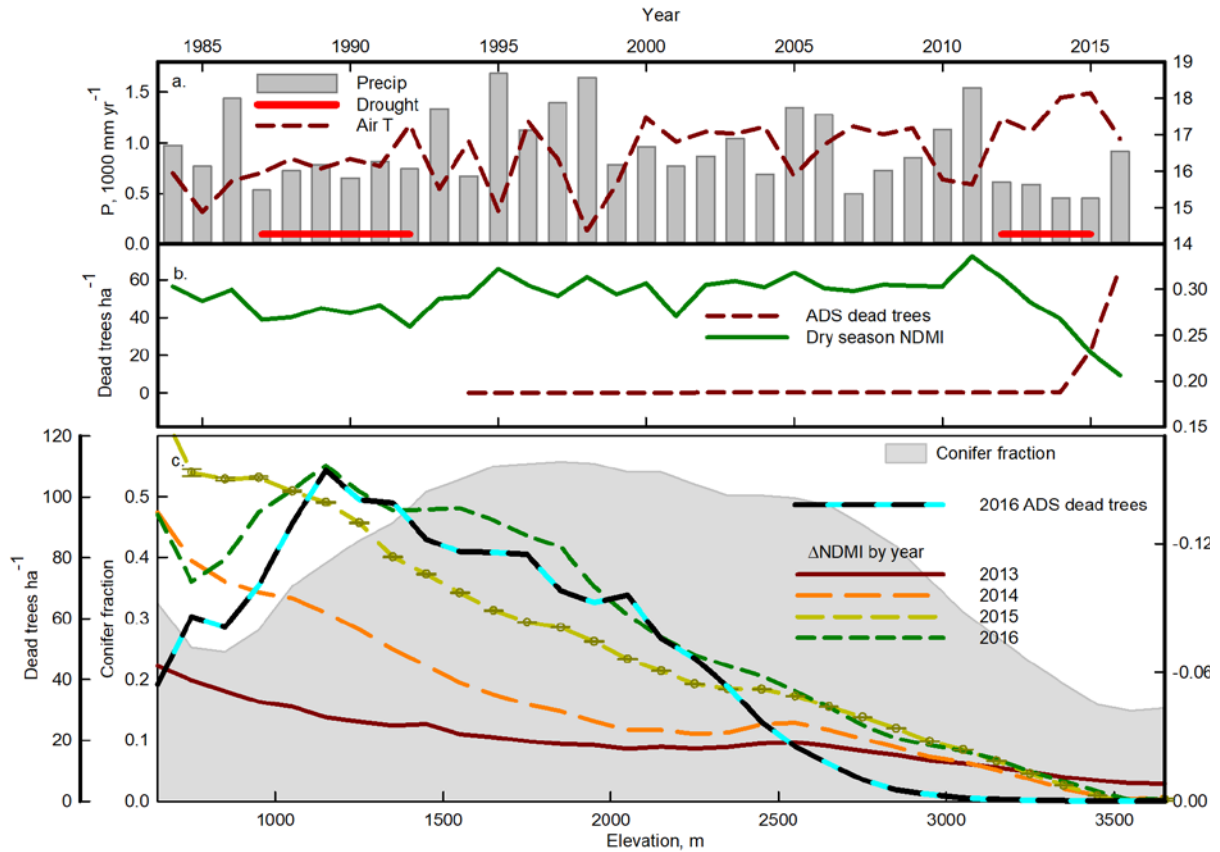
Figure 1. (a) Annual Water Year (Oct-Sept) cumulative precipitation (*P*) and mean maximum temperature (T_{max}) in southern Sierra Nevada from PRISM; horizontal red bars indicate extended droughts. (b) USFS Aerial Detection Survey dead trees ha^{-1} (ADS dead trees) and late dry-season Normalized Difference Moisture Index (Dry season *NDMI*; August-October). (c) Southern Sierra elevation patterns of July and August 2016 dead trees per ha (ADS dead trees), fractional conifer ground coverage (Conifer fraction), and late dry-season □*NDMI* for 2013 to 2016 relative to 2009-2011. Error bars for 2015 *ΔNDMI* are 95% confidence intervals.
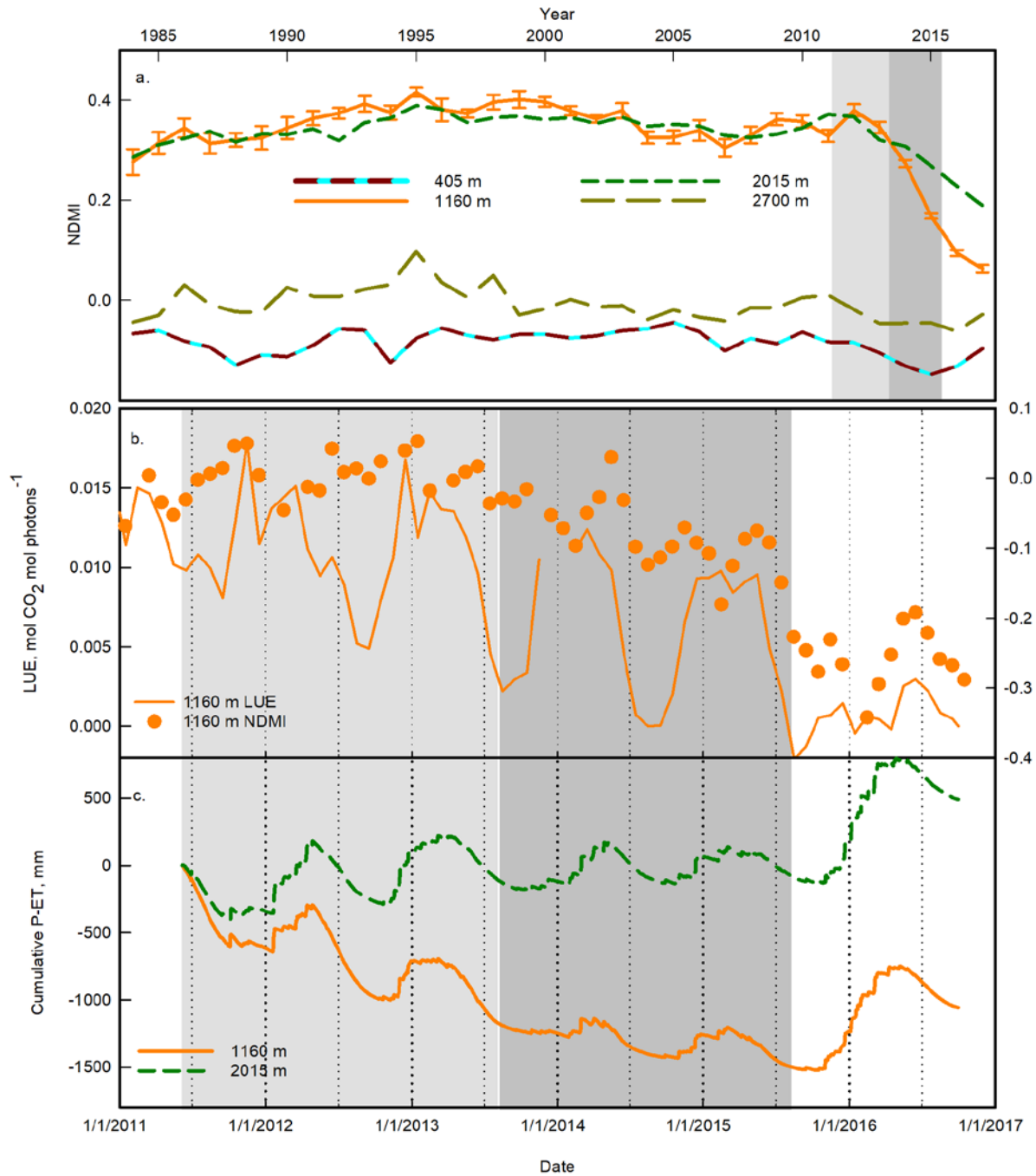
Figure 2. (a) Late dry-season Normalized Difference Moisture Index (*NDMI*) at focal sites. 95% confidence intervals based on spatial variation shown for 1160 m; confidence intervals at other sites are similar. (b) Photosynthetic whole-ecosystem light-use-efficiency at 1160 m (*LUE*; CO_2 uptake divided by incident light; solid lines connect monthly means) and monthly seasonally detrended *NDMI* (filled circles). (c) Cumulative water balance at 1160 and 2015 m (solid lines connect daily observations). Light gray (6/2011 to 8/2013) is the main period of moisture overdraft (the *drying phase*); dark gray (8/2013 to 8/2015) is the period of obvious vegetation decline (the *stress phase*).
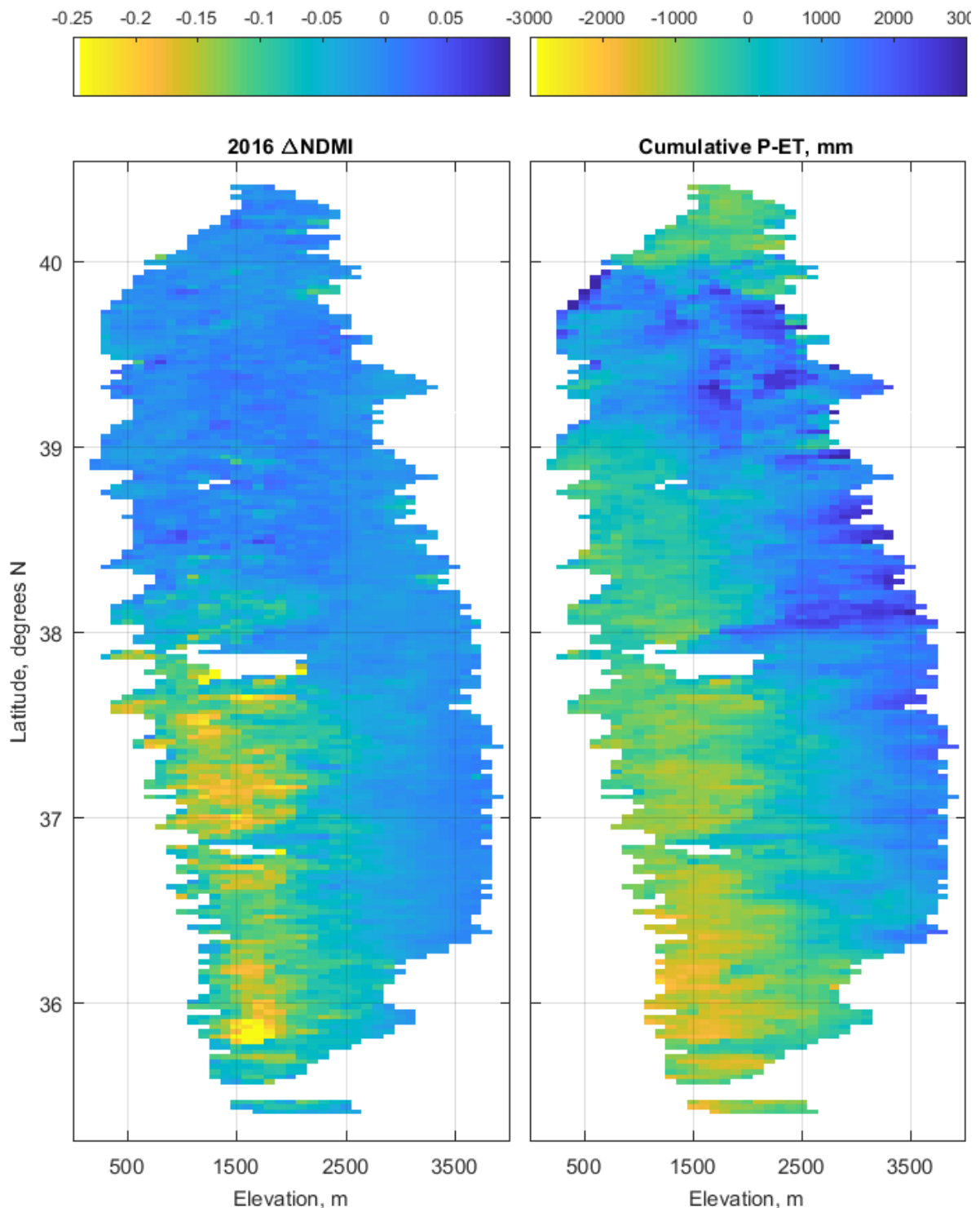
Figure 3. (a) Change in late dry-season Normalized Difference Moisture Index (*NDMI*) over the drought (□*NDMI*; 2016 *NDMI* minus 2009-2011) binned by latitude and elevation. (b) Cumulative *P-ET* over 2012-2015. Units are (a) □*NDMI* with negative indicating a greater *NDMI* drop and (b) mm, with negative indicating greater overdraft. Canopy dieback and cumulative *P-ET* overdraft were greatest at 35.7° to 37.65° latitude and below 2300 m elevation.
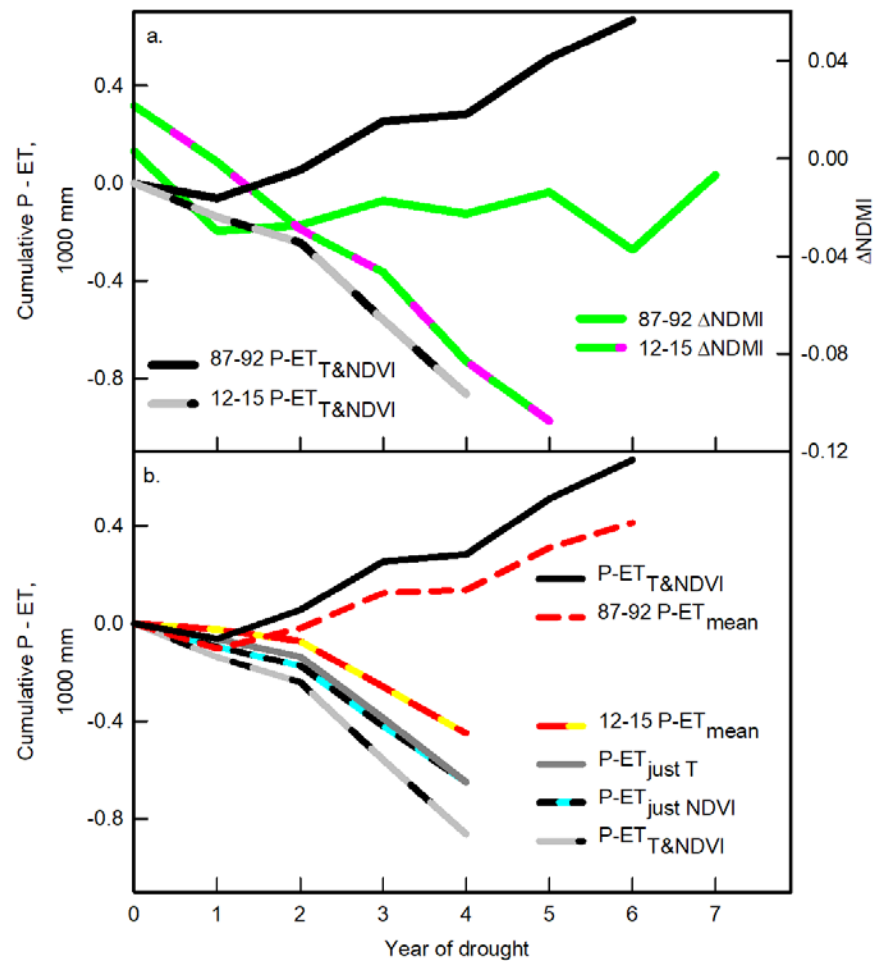
Figure 4. (a) Cumulative *P-ET* and July-Sept □*NDMI* for 1987-1992 and 2012-2015 droughts. (b) Comparison of cumulative *P-ET* calculated using four alternative approaches for 1987-1992 and 2012-2015 droughts (see also Fig. S10). *P-ET* in (b) was calculated using the observed *P* time series (PRISM), with *ET* calculated: i) as the mean *ET* averaged across all pixels and all years (*ET_mean*); ii) considering only *NDVI* (*ET_just NDVI*); iii) considering only the normalized saturated vapor pressure calculated from T_max (*ET_just T*); and iv) considering both vapor pressure and *NDVI* (*ET_T&NDVI*).

Methods

Ground-based measurements. *Tree death.* Ground-based measurements at the four core Southern Sierra Critical Zone Observatory sites[20] were focused in 200 × 50 m (1 ha) plots that extended 150 m in the mean daytime upwind direction and 50 m downwind of the eddy covariance towers[39]. Trees were tagged and stem diameter at breast height (dbh) was measured by species in summer 2009 or 2010 for all individuals with dbh > 0.10 m. The plots were revisited in summer 2016, the tagged trees relocated and recorded as dead or alive, and the fraction of basal area that had died was calculated. Not all of the original tags were found during the resurveys and the 2016 live basal area was corrected assuming the mortality rate of "missing" trees matched that of the resurveyed individuals.

Eddy covariance fluxes. We measured the net CO_2 exchange and evapotranspiration (*ET*) at four eddy-covariance towers in and around the upper Kings River basin along a west to east transect at ∼800 m elevation intervals beginning at 405 m. These towers were located in an area where the 2012-2015 CA drought was especially severe. Methodological details and site descriptions are provided in reference[20].

Cumulative, monthly and annual CO_2 exchange and *ET* (Fig. 2bc, S4, S6) were calculated by integration after filling intervals with missing, calm, or otherwise unsuitable observations as a function of incoming solar radiation. The cumulative and monthly exchanges were corrected for the lack of energy budget closure at each site[40]. Gross Ecosystem CO_2 exchange was calculated as the half-hour daytime net CO_2 exchange minus the estimated daytime respiration rate. Daytime respiration was estimated at ten-day intervals from the zero-light intercept of the Net CO_2 exchange light curve. The monthly photosynthetic light use efficiency (*LUE*) was calculated as the monthly cumulative gross CO_2 divided by the cumulative incident photosynthetically active photon flux.

The cumulative water balance (Fig. 2c) was calculated by integrating the observed precipitation and *ET* observations. *P* at 1160 m was measured with a tipping bucket gauge; nearly all *P* at 1160 m falls as rain, and the time series of *P* at 1160 m agreed well with observations from other weather stations in the area. *P* at 2015 m was obtained from the National Atmospheric Deposition Program (NADP) station CA29—Kings River Experimental Watershed, which is 1.2 km southeast of the eddy-covariance tower and at the same elevation. Periods with missing NADP *P* data were filled using observations from the Dinkey Creek Remote Automated Weather Station (RAWS), which is 3.4 km east of the eddy covariance tower.

The relationship between air temperature and half-hour *ET* (Fig. S5) was determined before the onset of the 2012-2015 drought (spring and early summer during 2011 and 2012). Half hour observations with an incoming solar radiation above 200 Wm^{-2} were sorted into 1°C wide bin and the means and 95% confidence intervals calculated based on the variation within bins. The normalized change in saturated vapor pressure with T was calculated with the Antoine equation.

Data from six additional flux towers in Southern California were combined with the SSCZO towers to create a regression between annual *ET* and the Normalized Difference Vegetation Index (*NDVI*) to spatially and temporally extrapolate *ET* (Fig. S6, ref [20]). The *NDVI*s used for this regression were calculated using the same algorithm used to calculate *NDVI* across the entire Sierra Nevada.

We have discussed our *ET* regression approach in previous papers[13,20,24]. A strong correlation exists between annual *NDVI* and *ET* as a consequence of bi-directional linkages between Leaf Area Index (*LAI*) and canopy gas exchange. A site's water balance, *LAI*, primary production, and annual *ET* are tightly correlated through a series of feedbacks in semi-arid regions[41,42]. A high annual *LAI* both drives a high annual *ET* and is symptomatic of a high annual *ET*. In turn, *LAI* is well correlated with the Normalized Vegetation Difference Index (*NDVI*)[43], creating a tight relationship between annual *NDVI* and *ET* (Fig. S6). The relationship between annual *NDVI* and *ET* is much stronger than the relationship between hourly *NDVI* and *ET*. The hourly relationship is uni-directional (it mainly reflects the effect of *LAI* on *ET*), and is confounded by fluctuations in meteorological conditions, stress, plant physiology and phenology[44]. Regression approaches provide an excellent strategy for estimating annual *ET*, but are unsuitable for quantifying day-to-day or seasonal patterns of *ET*, when more biophysical strategies are required.

Geographic information system and raster datasets.
General. All geospatial analyses used co-registerered raster layers at 0.0002695° resolution for a 23000 by 19000 pixel region, with the upper left corner at -122°, 41°, WGS84. Analyses were done in ArcGIS, ENVI and Matlab, with ArcGIS toolbox and ENVI used to reproject and rasterize vector datasets and Matlab used to process the Landsat imagery and analyze the datasets.

Digital elevation map. We used the 2013 version USGS NED 1 arc sec Digital Elevation Map (DEM) from https://viewer.nationalmap.gov/basic/.

USFS mortality: We used the main (midsummer) Aerial Detection Survey of forest health for the USFS Region 5 from https://www.fs.usda.gov/detail/r5/forest-grasslandhealth/?cid=fsbdev3_046696. We reprojected the vector-based surveys, and rasterized the dead trees per acre and area flown fields. We then calculated an annual raster layer of dead trees that combined the observed mortality and flown layers, inserting zero for pixels that were flown and did not report dead trees. We then estimated the mortality for each pixel during the drought as the maximum number of dead trees observed at a location across the main summer surveys during 2013 to 2016.

USFS Existing Vegetation: We used the ExistingVegSouthSierra2000_2008_v1.gdb and ExistingVegR5_NorthSierra2000_2014_v1.gdb databases from https://www.fs.usda.gov/detail/r5/landmanagement/resourcemanagement/?cid=stelprdb5347192. We mosaiced the datasets and reprojected and rasterized the WHR class and CON_CFA fields.

T_{max} and P: We used the monthly time series of daily maximum temperature and precipitation at 4-km resolution for 1981-2016 from the Parameter-elevation Relationships on Independent Slopes Model (PRISM; http://prism.oregonstate.edu/recent/). We downsampled these layers to 0.0002695° by bilinear interpolation and summed or

averaged by WY. We used a similar approach for the PRISM 1981-2010 T_{max} and P Normals at 800-m resolution.

PDSI, SPI and SPEI: We used the monthly time series of Palmer Drought Severity Index (*PDSI*), 48-month Standardized Precipitation Index (SPI) and 48-month Standardized Precipitation Evapotranspiration Index (*SPEI*) at 4-km resolution for 1981-2016 from the West Wide Drought Tracker (https://wrcc.dri.edu/wwdt/). We downsampled these observations to 0.0002695° by bilinear interpolation and averaged for June-August of each year.

Fire history: We used the fire history GIS data set from the California's Fire and Resource Assesment Program (FRAP; http://frap.fire.ca.gov/data/statewide/fire17_1.zip. We reprojected and then rasterized the most recent year of burn.

Landsat: All Collection 1, Level 1 Landsat 5, 7, and 8 Surface Reflectance and Brightness Temperature images with less than 30% cloud cover for WRS2 Path/Row 41035, 42034, 42035, 43033, 43034, 44032 were downloaded from USGS (https://espa.cr.usgs.gov) after reprojection at 0.0002695° resolution. The Landsat Collection 1 datasets represent a milestone in remote sensing science, with comparatively stable radiometric calibration[45], and atmospheric correction[46]. Some additional biases in vegetation indices remain[47-49], which we corrected by linear regression based on temporally adjacent *NDVI* and *NDMI* observations in California (see regressions below). The resulting linear regressions, which tied L5 and L8 to L7, yielded similar results to those reported previously[47-49]. Likewise, the Landsat Collection 1 pixel quality data layers represent a milestone, though visual examination of imagery for our study area indicated the masks occasionally missed areas with snow, low level clouds and cloud shadows. We consequently further masked the imagery after ingesting the full Landsat time series for a location to remove pixels that were anomalously cold and also either anomalously dark or bright[50].

We examined our time Landsat series for possible step changes during periods that have been identified as problematic. In particular, we focused on shifts in L5 during 1995 relative to 1994 and 1996 with orbital anomalies[51]; a step change in 2000 with the initiation of L7; a step change in 2003 with L7 SLC failure; a step change in L5 around 2005 with an orbital shift; a step change in 2011 with L5 termination; and a step change in 2013 or 2014 with L8 initiation. Our time series analysis did not show anomalies that coincided with these suspect periods, and the main vegetation shifts we identified (1994 to 1996, 2009 to 2012 and 2014 to 2016 in Figs 1b, 2a and S10a) did not coincide with known anomalies in the satellite record.

We further examined the separate time series for each Landsat instrument after homogenization and confirmed that the interannual and mean summer NDVIs and NDMIs during overlapping periods were in good agreement (Fig. S12). The mean L5 summer NDVI for the pixels that met the criteria used in Fig. 4 was 0.654 during 2000 to 2011, while the corresponding L7 NDVI was 0.648. The mean L5 summer NDMI was 0.294, while the corresponding L7 NDMI was 0.293. The agreement between L7 and L8 was not quite as good, with a mean L7 NDVI of 0.596 during 2013 to 2016 compared to a L8 mean of 0.614, and a L7 mean NDMI of 0.239 compared to a L8 mean of 0.232. These residuals are

small in absolute terms (a few percent), and similar to those that have been reported in previous studies.

Normalized Difference Indices, such as *NDVI* and *NDMI*, are largely insensitive to illumination differences with slope and aspect, and we consequently did not correct for topography.

Canopy dieback and ET derivation from Landsat: We used the late growing season (August to October) Landsat Normalized Difference Moisture Index (*NDMI*; (NIR-SWIR1)/(NIR+SWIR1)) to quantify evergreen canopy dieback. *NDMI* is well correlated with the live leaf area in a pixel. Hydrated leaves are dark in the ShortWave InfraRed (SWIR) with moisture absorption and bright in the Near InfraRed (NIR) with light scattering. Leaf and canopy mortality reduce NIR reflection, SWIR absorption and *NDMI*. *NDMI* is not unique in its ability to detect leaf and canopy mortality and alternative indices and approaches that emphasize NIR reflection and SWIR absorption have also proven effective[15-19]. Our annual late-growing-season *NDMI* data layers were highly correlated with previously reported summer canopy water contents based on a machine-learning fusion of airborne observations and Landsat[11,52].

Forest die-off in the Sierra Nevada was greatest among conifers, and our focus on August to October imagery allowed us to better isolate the year-to-year changes in evergreen canopies. Deciduous vegetation in California's Mediterranean climate is typically tied to winter and spring precipitation, with senescence occurring shortly after the onset of the summer dry season. Wet years in California cause a large expansion of spring deciduous vegetation. Spring *NDMI* (March to June) therefore reflects interannual variation in deciduous vegetation including herbs, as well as longer-term patterns of evergreen and deciduous perennial density. Most of the *LAI* in the late summer is evergreen, and year-to-year shifts in August to October *NDMI* provide a focused signal of evergreen canopy loss or expansion.

NDVI and *NDMI* both incorporate NIR reflectance, respond positively to canopy density and consequently are correlated, raising the risk that our comparison of *P-ET* with $\square NDMI$ is not mathematically independent. However, *ET* calculated from annual *NDVI* was weakly correlated with $\square NDMI$ across latitude and elevation (i.e., a comparison similar to those in Fig. S2 found an R^2 of 0.11 between *ET* and $\square NDMI$), and much of this relationship may reflect the biophysical tendency for greater mortality in locations with denser canopy, as opposed to a mathematical artifact. We conclude the relationship we found between *P-ET* and $\square NDMI$ (Fig. S2c) is not driven by an underlying mathematical correlation between *NDVI* and *NDMI* for four main reasons. First, we found a much tighter, non-linear relationship between *P-ET* and $\square NDMI$ than between *ET* alone and $\square NDMI$. Second, our analysis focused on $\square NDMI$ rather than NDMI alone. Third, we found a similarly tight relationship between *P-ET* and ADS mortality (Fig. S2b), which are fully independent measures. Fourth, *NDVI* and *NDMI* are not perfectly correlated, and were averaged over different periods of the year.

Processing steps: The Landsat imagery was processed through the following steps:
1) The Tasseled Cap brightness, Normalized Difference Vegetation Index (*NDVI*; (NIR-Red)/(NIR+Red)) and

Normalized Difference Moisture Index (*NDMI*; (NIR-SWIR1)/(NIR+SWIR1)) were calculated for all images.

2) Images were masked for cloud, cloud shadow or snow using the USGS pixel_qa layer.

3) Images were cut and sorted to 0.2695° by 0.2695° tiles.

4) The full time series for each 0.2695° by 0.2695° tile was stacked and further masked for pixels that were both anomalously cold and anomalously dark or bright (see also ref[50]).

5) Observations of *NDVI* and *NDMI* from Landsat 5 and 8 were homogenized to Landsat 7 using regressions determined by comparing consecutive observations (see also refs [47-49]):
L7 *NDVI* = L5 *NDVI* * 1.0630 - 0.0096
L7 *NDVI* = L8 *NDVI* * 0.9553 - 0.0232
L7 *NDMI* = L5 *NDMI* * 1.0015 - 0.0076
L7 *NDMI* = L8 *NDMI* * 0.9852 - 0.0260

6) A larger stack that included the dates (layers) for all possible L5, 7 and 8 overpasses was created, populated with the observed values, and filled by linear interpolation along the time axis.

7) The annual and seasonal means for each water year (Oct-Sept) were calculated.

8) The individual 1000 by 1000 pixel tiles were mosaiced to the full 23000 by 19000 pixel study area.

9) *ET* was calculated for each pixel and water year from the annual mean *NDVI* using the regression in Fig. S6. *P-ET* was calculated for each pixel and water year by subtracting *ET* from the down-sampled PRISM *P*.

Additional details on plots. *Figure 1*. All panels were calculated for 35.69°-37.65° latitude and at or below 2300 m elevation; this band is centered on the SSCZO, and was selected to include the area with the greatest *P* shortfall and dieback. All data were screened to exclude locations with a wildfire since 1980, or that were not conifer dominated (only used WHR types SMC, PPN, MHC, LPN, RFR, WFR, SCN, JPN, DFR, EPN, PJN), or that had a 30 year Normal *P* of less than 600 mm. Dead trees in (b) and (c) were calculated from the main (mid-summer) ADS vector layers. Altitudinal patterns in (c) were calculated as means for 100-m elevation bins for July and August 2016 dead tree inventories by the USFS Aerial Detection Survey. The mean conifer cover was calculated from the USFS Existing Vegetation (EVeg). The change in late dry-season *NDMI* for each year is relative to the *NDMI* before the drought (2009-2011 mean). Bins were screened to exclude n < 1000. Error bars for 2015 □*NDMI* are 95% confidence intervals based on variation within a bin (n > 10^4 at mid elevation).

Figure 2, (a) Points are averages for 9 Landsat pixels (a 90 by 90 m area) in the mean upwind direction from the tower for August to October of each year. The 95% confidence intervals based on the variation among Landsat pixels is shown for the 1160 m site; the confidence intervals at the other sites were similar. *NDMI* provides a measure of the density of living leaves, and the focus on the late drought period from August to October targets the contribution of evergreen foliage. (b) The monthly Light Use Efficiency was calculated as the monthly gross CO_2 uptake from eddy covariance per incident photosynthetically active photon flux. The monthly seasonally-detrended *NDMI* was calculated as the observed NDMI calculated by interpolation and averaging minus the mean NDMI observed for that month during 1984-2012. (c) Cumulative water balance was calculated as the sum of precipitation (*P*) measured by local gauges minus Evapotranspiration (*ET*) measured by eddy covariance in mm starting 6/6/2011 (the last day with meaningful *P* in the 2010-11 WY).

Figure 3. (a) Patterns of tree dieback based on □*NDMI* (Aug-Oct 2016 minus Aug-Oct 2009-2011) and (b) cumulative *P-ET* during 2012-2015 WYs as a function of latitude (y axis, degrees N) and elevation (x axis, meters above sea level). A three year pre-drought reference period (2009-2011) was used to reduce the influence of interannual variability. All pixels were screened to exclude locations that burned since 1980, or were not conifer dominated (only used WHR types SMC, PPN, MHC, LPN, RFR, WFR, SCN, JPN, DFR, EPN, PJN), or had a mean 30 year precipitation less than 600 mm. Colors indicate the average □*NDMI* (negative indicates a greater *NDMI* drop over time) and 2012-2015 WY cumulative *P-ET* (mm; negative indicates a greater overdraft) for 100 m elevation and 0.02695° latitude bins. Scatterplot and best fit regression between □*NDMI* binned by latitude and elevation (Fig. 3a) and corresponding cumulative *P-ET* (Fig. 3b) is shown in Fig. S2c (R^2 = 0.5953).

Figure 4. (a) □*NDMI* for the 1987-1992 and 2012-2015 droughts was calculated as the Aug-Oct mean relative to the periods before drought (1984-1986 or 2009-2011). Three year pre-drought reference periods were used to reduce the influence of interannual variability. Cumulative WY *P-ET* was calculated from PRISM *P* minus the *NDVI*-based *ET* * normalized Saturated VP (Fig. S5). (b) Comparison of cumulative *P-ET* calculated for 1987-1992 and 2012-2015 droughts, with observed PRISM *P* and *ET* calculated using four alternative approaches. *ET* in (b) was calculated: i) as the mean *ET* averaged across all pixels and all years (ET_{mean}); ii) considering only interannual variability in canopy density as measured by *NDVI* (Fig. S6; $ET_{just\ NDVI}$); iii) considering only the effect of temperature on normalized saturated vapor pressure calculated from T_{max} ($ET_{just\ T}$; i.e., ET_{mean} * normalized saturated vapor pressure (Fig. S5)); and iv) considering the effects of both temperature on saturated vapor pressure and canopy density ($ET_{T\&NDVI}$; i.e., $ET_{just\ NDVI}$ * normalized saturated vapor pressure (Fig. S5)). All time series were calculated for 35.69°-37.65° latitude and at or below 2300 m elevation. All data were screened to exclude locations with a wildfire since 1980, or that were not conifer dominated (only used WHR types SMC, PPN, MHC, LPN, RFR, WFR, SCN, JPN, DFR, EPN, PJN), or that had a 30 year Normal *P* of less than 600 mm.

The fractional effect of warming on cumulative *P-ET* was calculated as (($P-ET_{just\ T} – P-ET_{mean}$)/ $P-ET_{mean}$). The fractional effect of structural overshoot on cumulative *P-ET* was calculated as (($P-ET_{just\ NDVI} – P-ET_{mean}$)/ $P-ET_{mean}$). The fractional effect of additional warming on *P-ET* during drought was calculated for 1 to 4°C incremental warming using the approach used to calculate the fractional effect of warming on cumulative *P-ET*. The fractional effect of additional warming on tree death was calculated by converting the *P-ET* calculated for 1 to 4°C to number of dead trees per hectare based on Fig. S2b.

Data availability
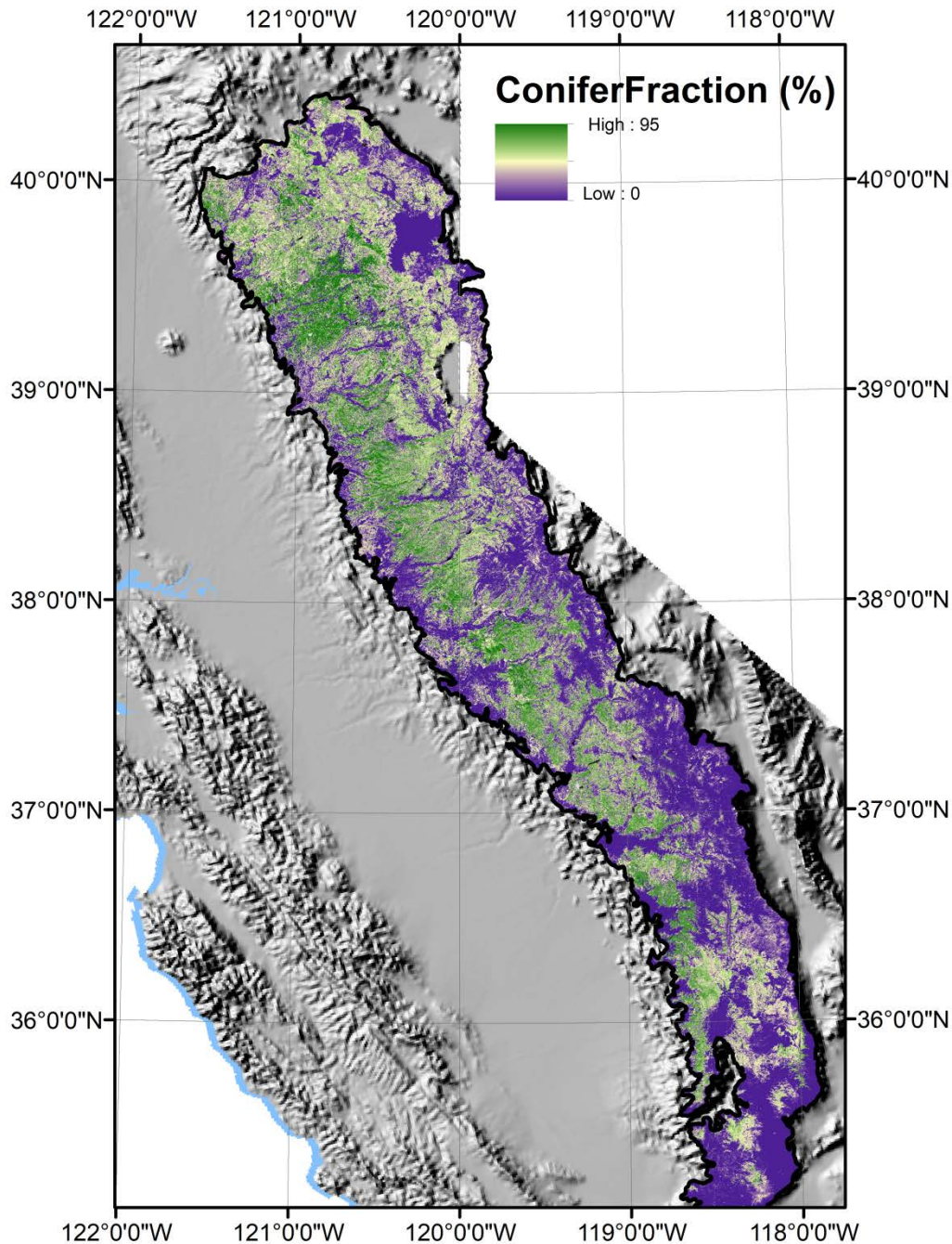
References

39. Kelly, A. E. & Goulden, M. L. A montane Mediterranean climate supports year-round photosynthesis and high forest biomass. *Tree Physiology* **36**, 459-468, doi:10.1093/treephys/tpv131 (2016).

40. Twine, T. E. *et al.* Correcting eddy-covariance flux underestimates over a grassland. *Agricultural and Forest Meteorology* **103**, 279-300, doi:10.1016/s0168-1923(00)00123-4 (2000).

41. Grier, C. C. & Running, S. W. Leaf area of mature northwestern coniferous forests - relation to site water-balance. *Ecology* **58**, 893-899, doi:10.2307/1936225 (1977).

42. Gholz, H. L. Environmental limits on above-ground net primary production, leaf-area, and biomass in vegetation zones of the pacific northwest. *Ecology* **63**, 469-481, doi:10.2307/1938964 (1982).

43. Carlson, T. N. & Ripley, D. A. On the relation between NDVI, fractional vegetation cover, and leaf area index. *Remote Sensing of Environment* **62**, 241-252, doi:10.1016/s0034-4257(97)00104-1 (1997).

44. Gamon, J., Field, C., Goulden, M. & al., e. Relationships between NDVI, canopy structure, and photosynthesis in 3 Californian vegetation types. *Ecological applications* **5**, 28-41 (1995).

45. Markham, B. L. & Helder, D. L. Forty-year calibrated record of earth-reflected radiance from Landsat: A review. *Remote Sensing of Environment* **122**, 30-40, doi:10.1016/j.rse.2011.06.026 (2012).

46. Masek, J. G. *et al.* A Landsat surface reflectance dataset for North America, 1990-2000. *Ieee Geoscience and Remote Sensing Letters* **3**, 68-72, doi:10.1109/lgrs.2005.857030 (2006).

47. Ju, J. C. & Masek, J. G. The vegetation greenness trend in Canada and US Alaska from 1984-2012 Landsat data. *Remote Sensing of Environment* **176**, 1-16, doi:10.1016/j.rse.2016.01.001 (2016).

48. Sulla-Menashe, D., Fried, M. A. & Woodcock, C. E. Sources of bias and variability in long-term Landsat time series over Canadian boreal forests. *Remote Sensing of Environment* **177**, 206-219, doi:10.1016/j.rse.2016.02.041 (2016).

49. Roy, D. P. *et al.* Characterization of Landsat-7 to Landsat-8 reflective wavelength and normalized difference vegetation index continuity. *Remote Sensing of Environment* **185**, 57-70, doi:10.1016/j.rse.2015.12.024 (2016).

50. Zhu, Z. & Woodcock, C. E. Automated cloud, cloud shadow, and snow detection in multitemporal Landsat data: An algorithm designed specifically for monitoring land cover change. *Remote Sensing of Environment* **152**, 217-234, doi:10.1016/j.rse.2014.06.012 (2014).

51. Zhang, H. K. & Roy, D. P. Landsat 5 Thematic Mapper reflectance and NDVI 27-year time series inconsistencies due to satellite orbit change. *Remote Sensing of Environment* **186**, 217-233, doi:10.1016/j.rse.2016.08.022 (2016).

52. Brodrick, P. G., Anderegg, L. D. L. & Asner, G. P. Forest Drought Resistance at Large Geographic Scales. *Geophysical Research Letters* **46**, 2752-2760, doi:10.1029/2018gl081108 (2019).

**Supplementary information:** Supplementary Figures 1–12

Figure S1a: California elevation (red to blue color ramp; meters above sea level) and Sierra Nevada ecoregion (open polygon). Elevation from USGS at 100 m resolution (https://www.sciencebase.gov/catalog/item/581d0539e4b08da350d52552). Sierra Nevada polygon from EcoregionsCalifornia07_3 (https://www.fs.fed.us/r5/rsl/projects/gis/data/calcovs/EcoregionsCalifornia07_3.html).
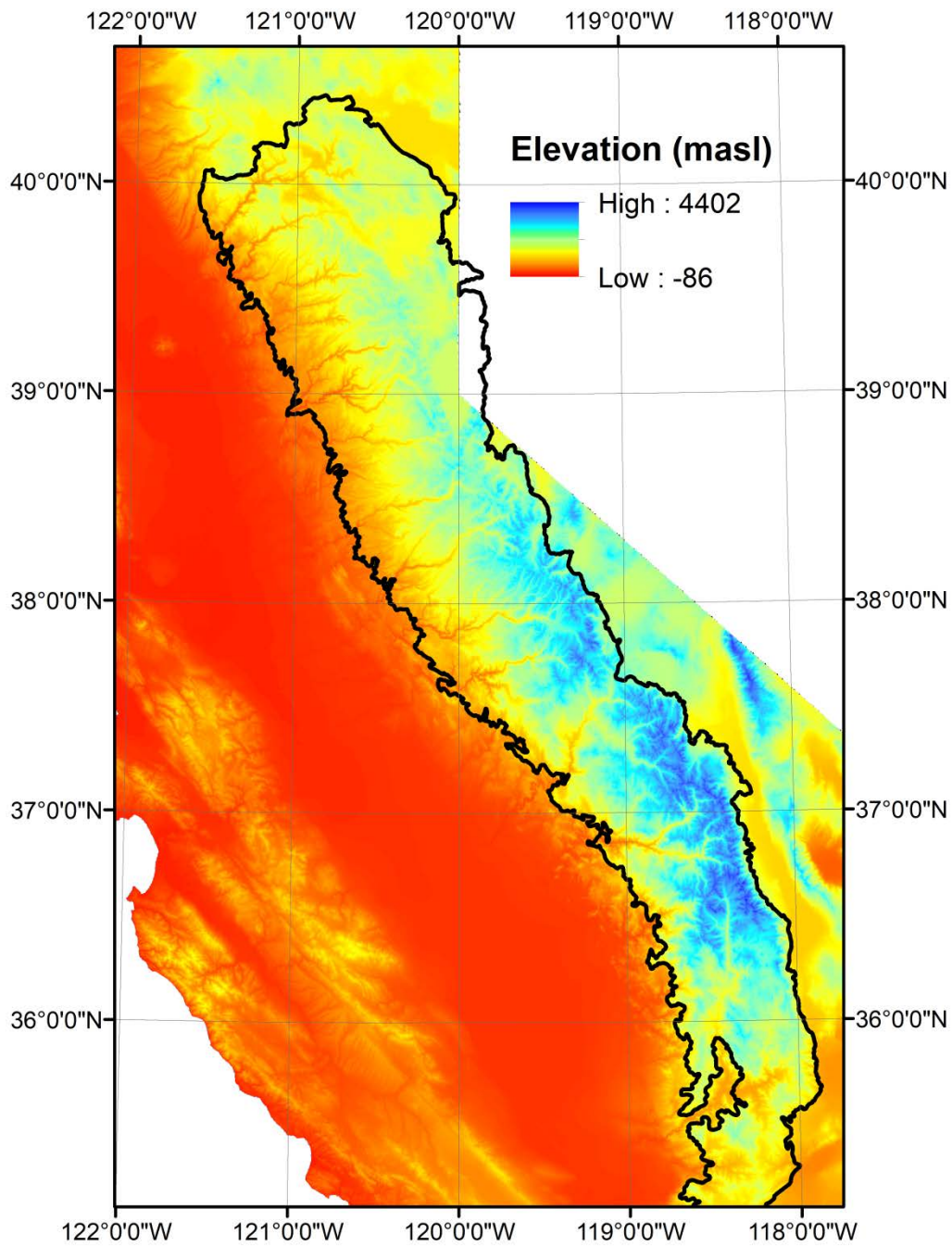
Figure S1b: Fraction conifer cover in a pixel (purple to green color ramp; percent) and Sierra Nevada ecoregion (open polygon; from EcoregionsCalifornia07_3). From CON_CFA in existingVegSouthSierra2000_2008_v1.gdb and ExistingVegR5_NorthSierra2000_2014_v1.gdb (https://www.fs.usda.gov/detail/r5/landmanagement/resourcemanagement/?cid=stelprdb534719). Background is shaded relief at 1 km from https://www.sciencebase.gov/catalog/item/4f4e4a60e4b07f02db63510b.

Figure S1c: Cumulative Precipitation minus Evapotranspiration over the drought (*P-ET* in mm summed over 2012-2015 water years; red to blue color ramp with negative numbers and warm colors indicating *P < ET* (a moisture overdraft and subsurface drying) and positive numbers and cool colors indicating *P > ET* (a moisture surplus and runoff generation)). *P-ET* was calculated from Landsat and PRISM. Sierra Nevada ecoregion shown as an open polygon. Background is shaded relief at 1 km resolution from
https://www.sciencebase.gov/catalog/item/4f4e4a60e4b07f02db63510b. Small sections in the south and northeast of the ecoregion were not included in the Landsat analyses. Lakes and water bodies were not included in the analysis.
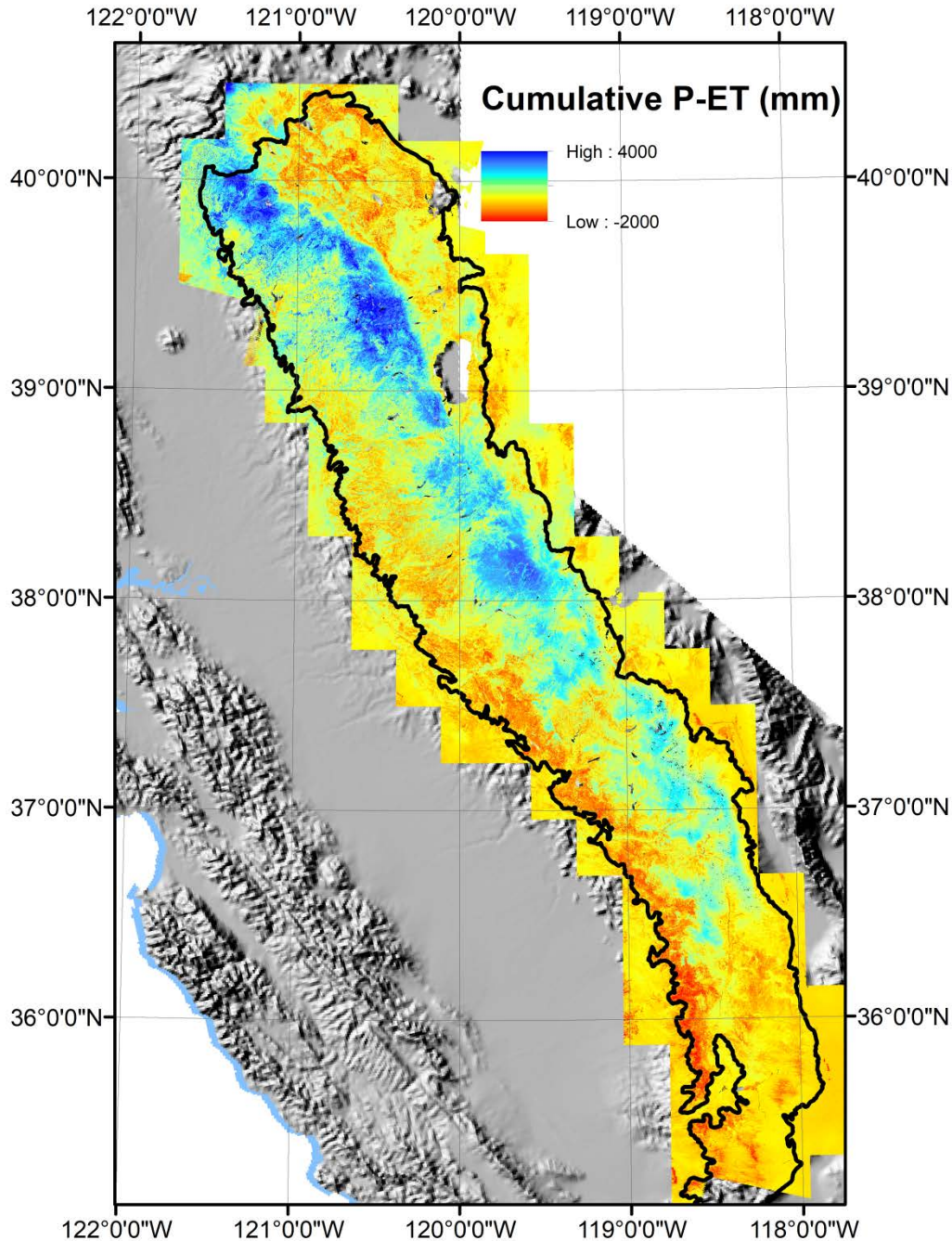
Figure S1d: Unmasked late dry-season Normalized Difference Moisture Index (*NDMI*; from Landsat) over the drought (*ΔNDMI*; 2009-11 *NDMI* minus 2016; green to brown color ramp where higher values indicating a greater *NDMI* decline and canopy dieback). Sierra Nevada ecoregion shown as an open polygon. Large areas of *NDMI* decline (red patches) were either recent fires (for example, the 2013 Rim Fire at 38°, -120°) or forest dieback. Large areas of NDMI increase (green patches) were typically earlier fires (for example, the 2007 Moonlight Fire at 40.3°, -120.7°).
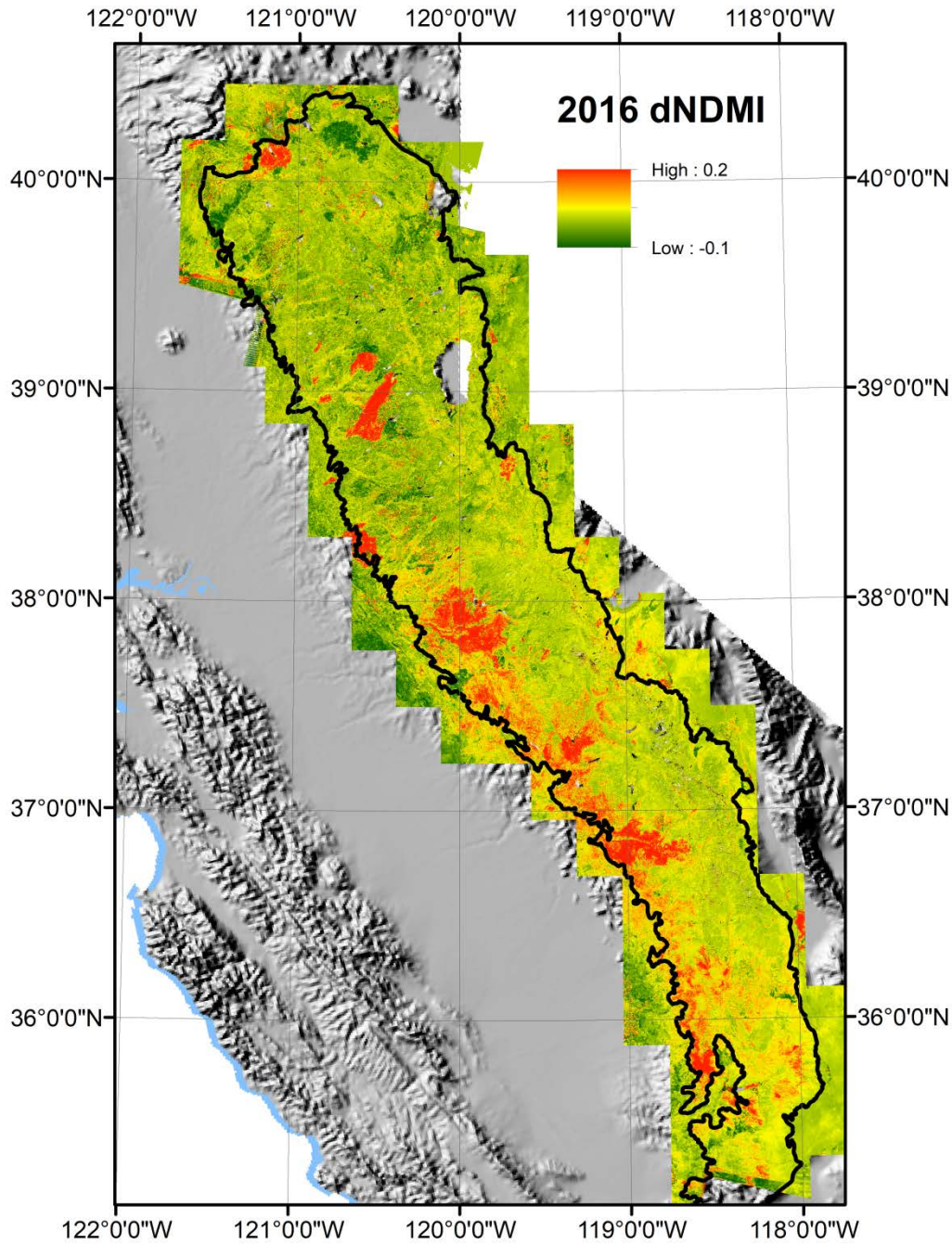
Figure S1e: Masked late dry-season Normalized Difference Moisture Index (*NDMI*; from Landsat) over the drought (*ΔNDMI*; 2009-11 *NDMI* minus 2016; green to brown color ramp where higher values indicating a greater *NDMI* decline and canopy dieback). Pixels were masked (shown as black) and excluded form analyses if they burned since 1980, or were not conifer dominated (only used WHR types SMC, PPN, MHC, LPN, RFR, WFR, SCN, JPN, DFR, EPN, PJN), or had a mean 30 year Precipitation less than 600 mm, or fell outside of the Sierra Nevada ecoregion. Background is shaded relief at 1 km resolution from https://www.sciencebase.gov/catalog/item/4f4e4a60e4b07f02db63510b.
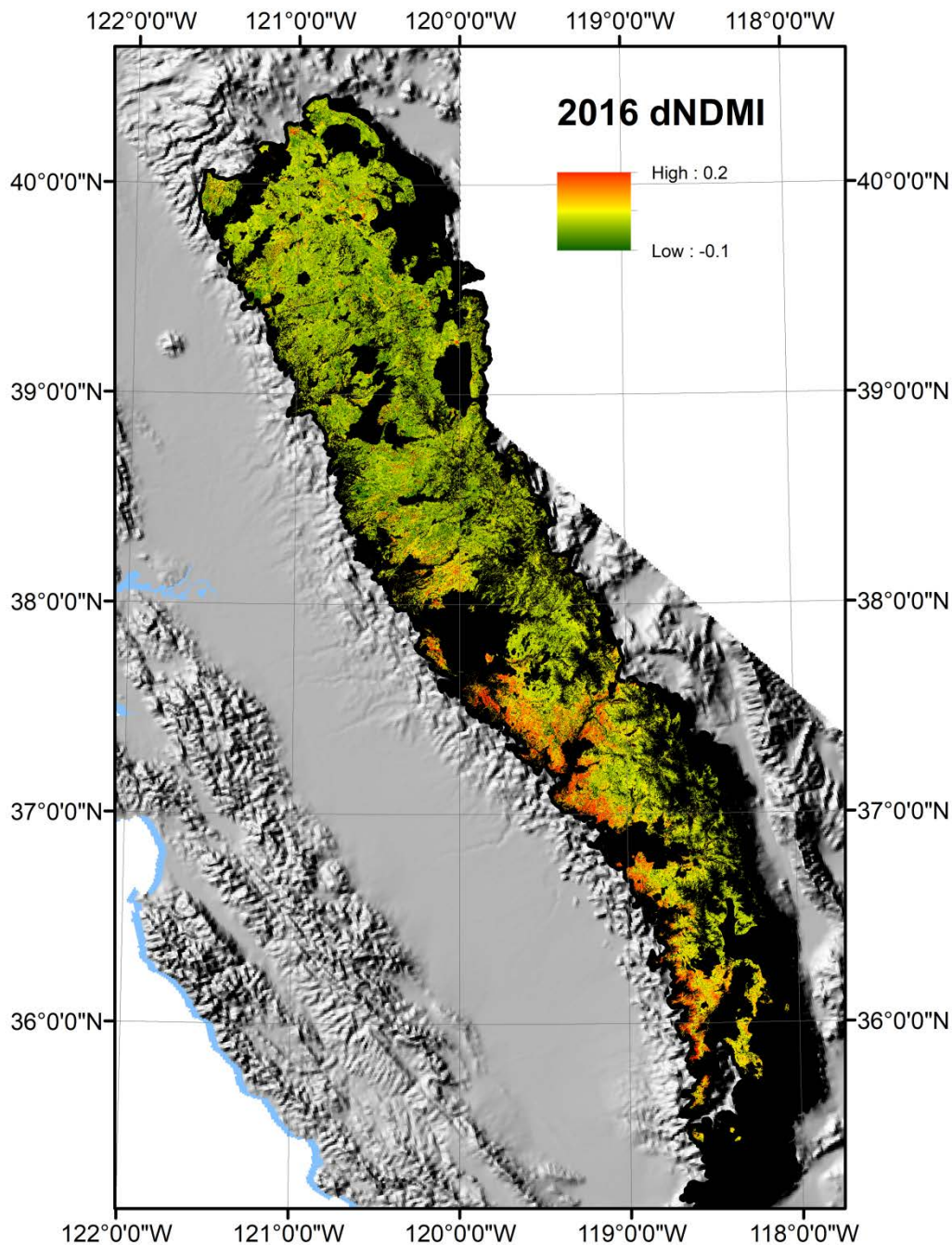
Figure S2: Relationship between USFS Aerial Detection Survey (ADS) dead trees per ha binned by latitude and elevation (from Fig. S3a) and (a) *ΔNDMI* (Fig. 3a), and (b) cumulative *P-ET* (mm, Fig. 3b). Relationship between *ΔNDMI* binned by latitude and elevation (Fig. 3a) and (c) corresponding cumulative *P-ET* (mm, Fig. 3b), (d) Palmer Drought Stress Index (*PDSI*, Fig. S7c), (e) Standardized Precipitation Index (*SPI*, Fig. S7a), and (f) Standardized Precipitation Evapotranspiration Index (*SPEI*, Fig. S7b). Best fit regressions are: (a) Dead trees per hectare = -0.4214-551.0 * (*ΔNDMI*); Rsqr = 0.5646. (b) for *P-ET* (mm) <= 131.7, Dead trees per hectare = -0.0499 * *P-ET* (mm) + 14.59; for *P-ET* (mm) > 131.7, Dead trees per hectare = -0.0047* *P-ET* (mm) + 8.636; Rsqr = 0.5128. (c) for *P-ET* (mm) <= 131.7, *ΔNDMI* = 0.0000737 * *P-ET* (mm) - 0.02987; for *P-ET* (mm) > 131.7, *ΔNDMI* = 0.00000646 * *P-ET* - 0.02101; Rsqr = 0.5953. (d) *ΔNDMI* = 0.0167 + 0.0164 **PDSI*; Rsqr = 0.1928. (e) *ΔNDMI* = 0.1313 + 0.0766 **SPI*; Rsqr = 0.3175. (f) *ΔNDMI* = 0.1546 + 0.0808**SPEI*; Rsqr = 0.2000.
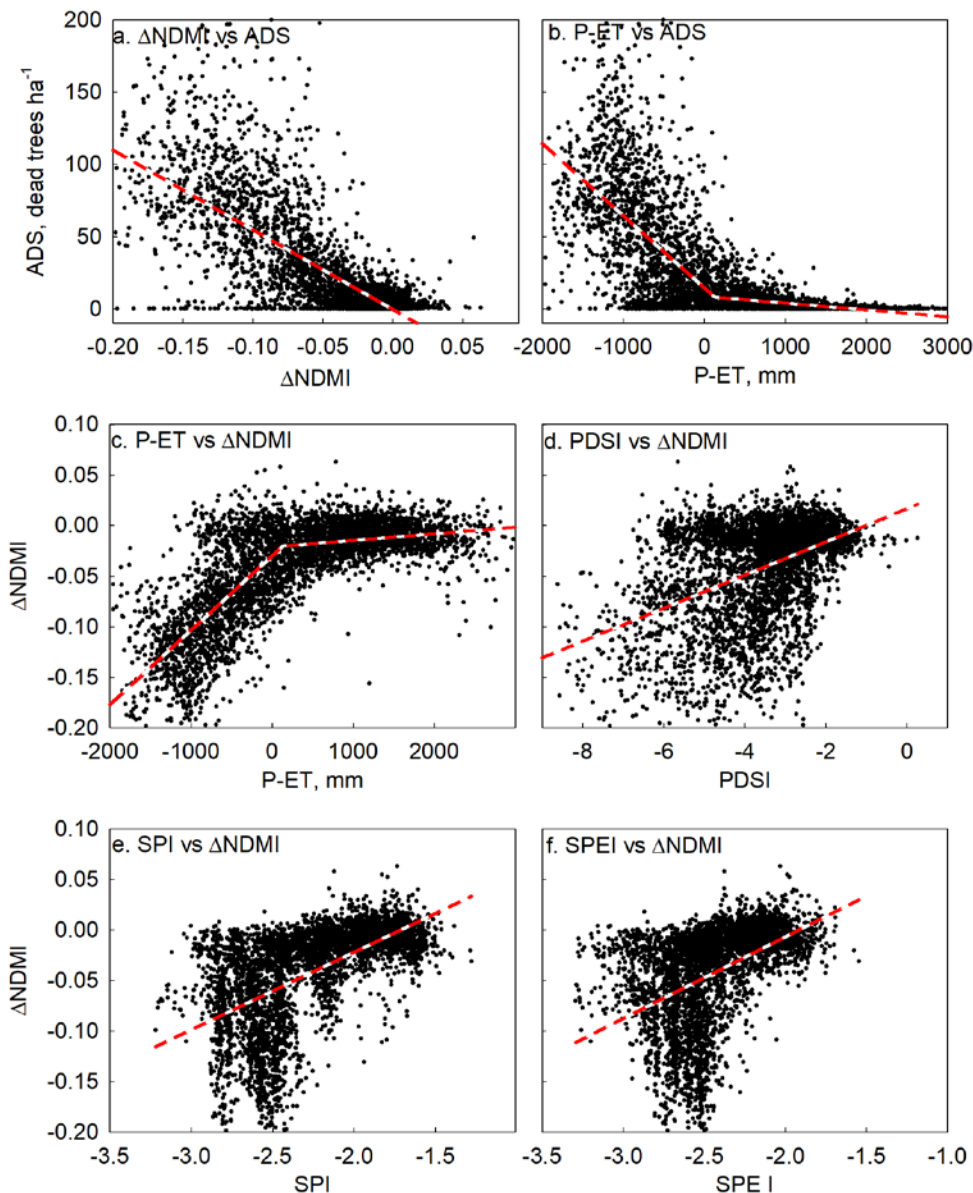
Figure S3: (a) Number of dead trees per hectare in main summer 2016 USFS Aerial Detection Survey (ADS) and (b) *ΔNDMI* in July-Sept 2016, as a function of latitude (degrees) and elevation (meters above sea level). Pixels were screened to exclude locations that burned since 1980, or were not conifer dominated, or had a mean 30 year *P* less than 600 mm. Pixels were binned at 100-m elevation and 0.02695°-latitude intervals and means calculated. Color ramps are above corresponding plots. Units are (a) mean number of dead trees per hectare reported by the ADS and (b) *ΔNDMI* with negative indicating a greater decline.
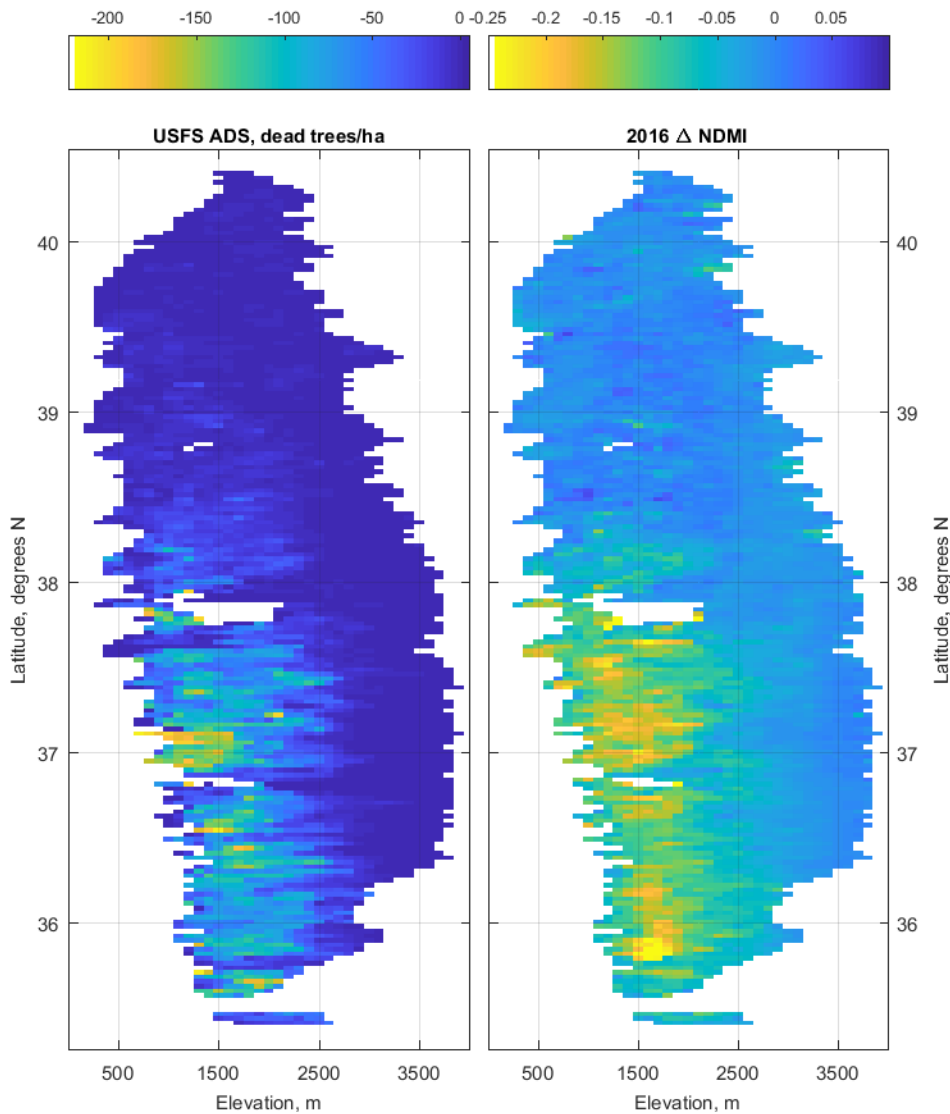
Figure S4: Gross CO$_2$ exchange at the (a) SSCZO 2015-m and (b) 1160-m elevation sites. Points show individual 30-minute Net CO$_2$ exchange and solid lines show mean monthly Gross CO$_2$ exchange (photosynthesis), with negative values indicating greater uptake. Solid vertical lines shows the start of the drought (6/2011) and the period of peak mortality at 1160 m (8/2015).
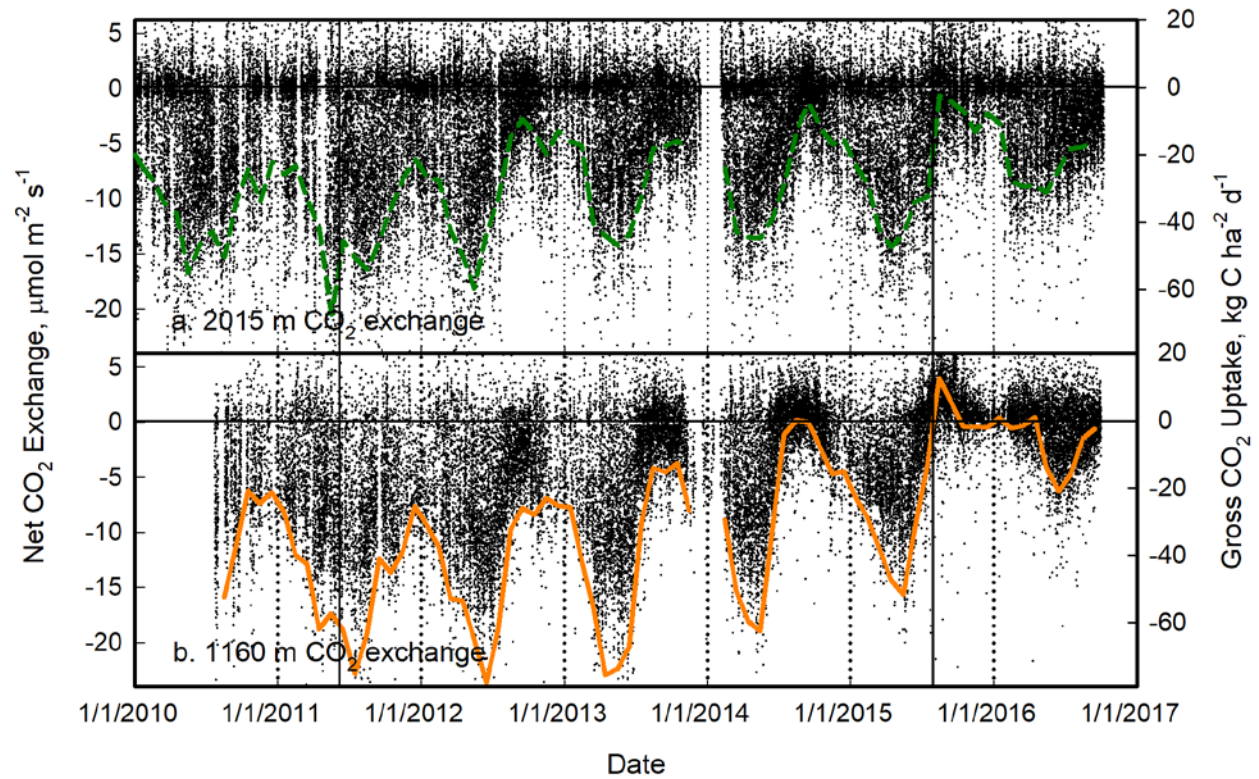
Figure S5: Relationship between half hour air T and half hour *ET* during sunny well-watered conditions before the onset of the 2012-15 drought (spring and early summer 2011 and 2012). Points are the mean *ET* with incoming solar radiation > 200 Wm^{-2} for 1°C bins. Error bars show the 95% confidence intervals based on variation within the bin (the confidence intervals were similar at the two sites). Large outlined symbols show the mean daytime temperature at each site. The filled line shows the relative vapor pressure for a given temperature from the Antoine equation.
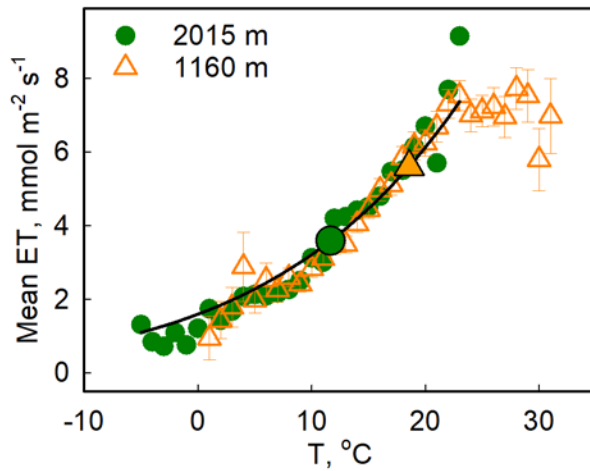
Figure S6: Annual water year *ET* by integrated eddy covariance against annual *NDVI* from Landsat for 9 nearest upwind pixels across multiple years at 10 California flux towers. Solid black line shows the best fit regression through all sites and for all years was *ET* (mm) = 117.16 * exp(2.8025**NDVI*) (R^2 = 0.8386). Symbols indicate individual sites as identified by the AmeriFlux site code (http://ameriflux.lbl.gov/sites). Thin lines show liner regressions based on interannual variability within each site. See ref[21] for details.
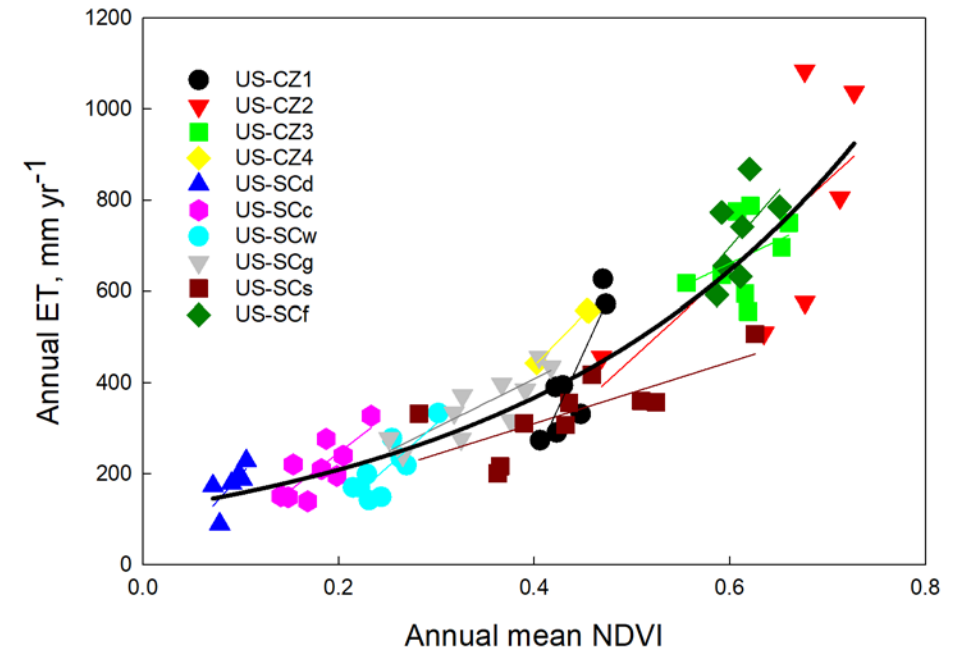
Figure S7: (a) 48-month summer (JJA) 2015 Standardized Precipitation Index (SPI), (b) 48-month summer 2015 Standardized Precipitation Evapotranspiration Index (*SPEI*) and (c) summer 2015 Palmer Drought Severity Index (*PDSI*) as a function of latitude (degrees N) and elevation (meters above sea level). Pixels were screened to exclude locations that burned since 1980, or were not conifer dominated, or had a 30-year Normal Precipitation less than 600 mm. Pixels were binned at 100 m elevation and 0.02695°-latitude intervals and means calculated. Color bars are above the corresponding plots. Units are (a) *SPI* with negative indicating less *P*, (b) *SPEI* with negative indicating less *P* or greater *ET*, and (c) *PDSI* with negative indicating more severe drought.
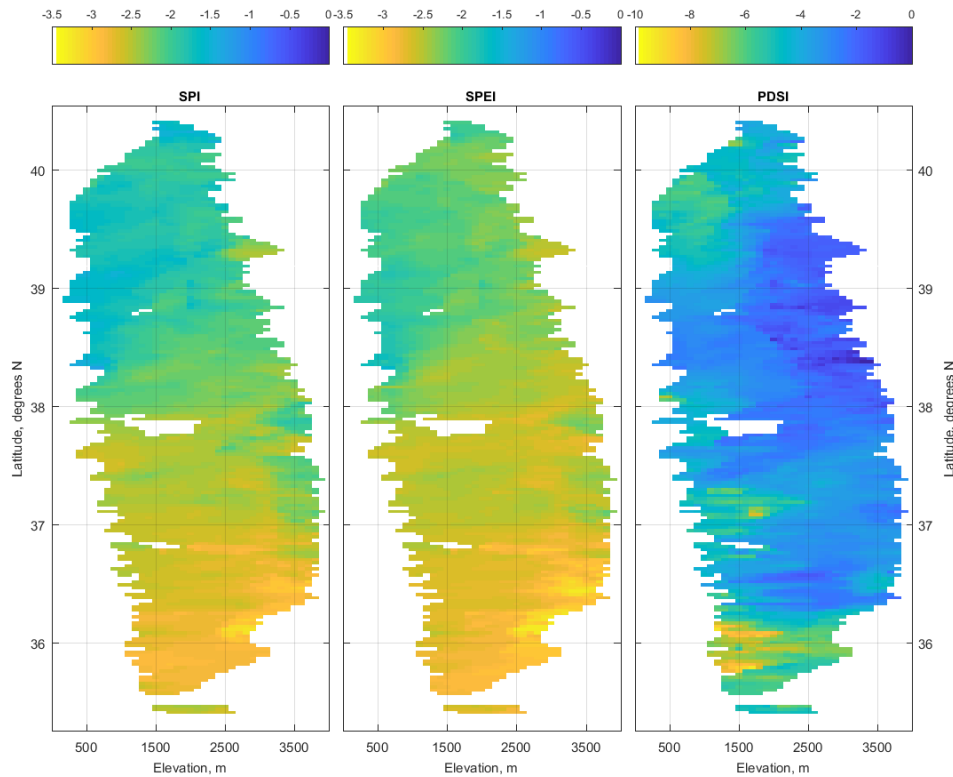
Figure S8: Elevation patterns of (a) 2016 *ΔNDMI*, cumulative 2012-15 *P-ET*, 2015 June to August *PDSI*, 2015 48-month *SPI* and *SPEI*, and (b) mean annual *ET* and *P* during 2012-2015. Pixels were screened for locations within 35.69 to 37.65 latitude, no reported fire since 1980, a 30-year Normal *P* of at least 600 mm yr^{-1} and a conifer dominated WHR class (e.g., only WHR types SMC, PPN, MHC, LPN, RFR, WFR, SCN, JPN, DFR, EPN, PJN). Pixels were binned and averaged at 100 m elevation intervals. Units in (a) *ΔNDMI* with negative indicating a greater drop in *NDMI* over time, *P-ET* in mm 4yr^{-1} where negative indicates a greater overdraft, 48 month summer *SPI*, *SPEI* or *PDSI*, where negative indicates lower *P*. Units in (b) are mm yr^{-1} averaged for 2012-15, where positive indicates greater *ET* or *P*. The area between the *P* and *ET* curves below ~2300 m elevation with *ET* > *P* in (b) corresponds to the negative *P-ET* in (a). The area between the *P* and *ET* curves above ~2300-m elevation with *ET* < *P* in (b) corresponds to positive *P-ET* in (a).
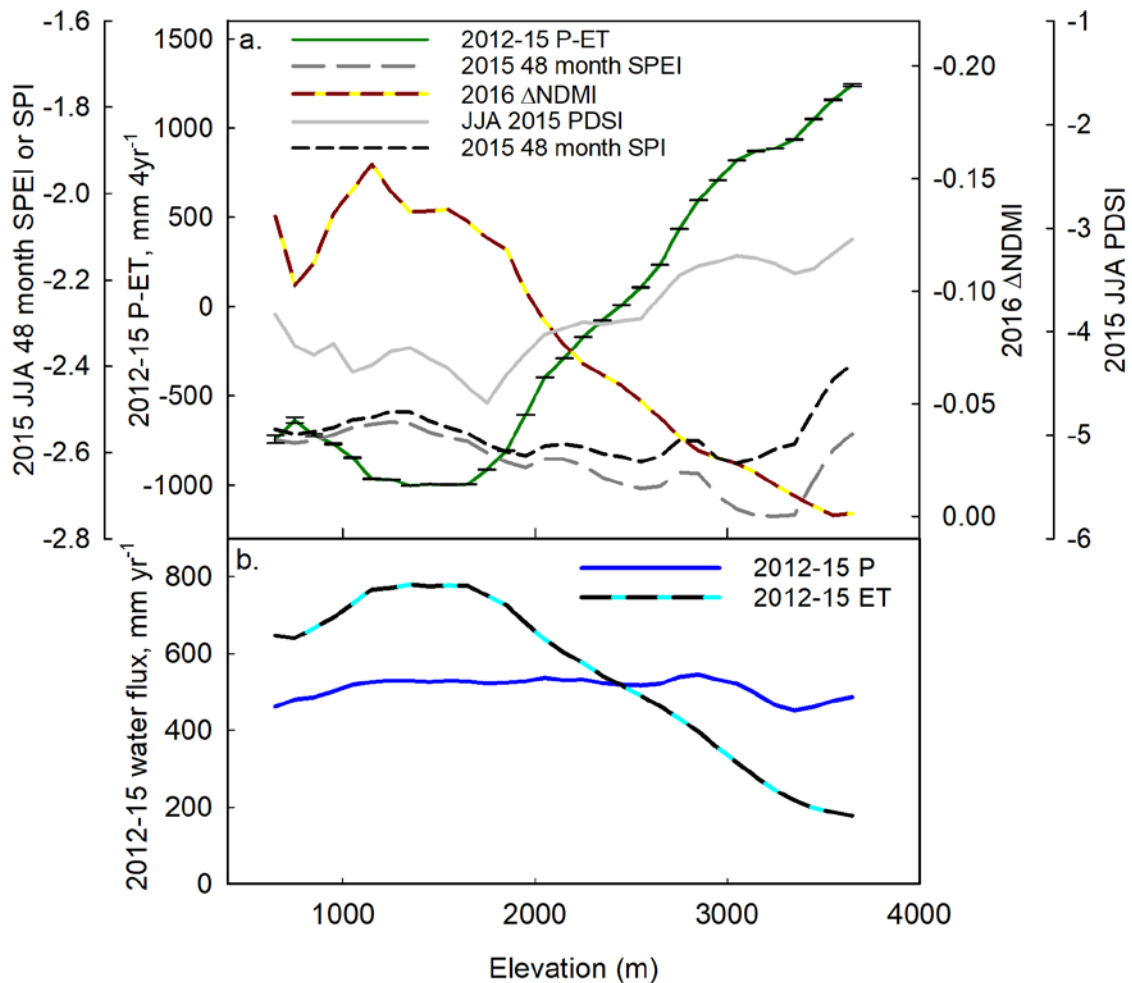
Figure S9: (a) the difference between 2009-2011 and 2016 *NDMI* ($\Delta NDMI$ with positive indicating a greater *NDMI* decline) and the number of dead trees reported by the USFS Aerial Detection Survey (USFS ADS, dead trees per ha) as a function of the local aspect (degrees with 90° indicating East facing slopes and 180° indicating South facing). (b) Normalized Difference Moisture Index (*NDMI*) during 2009-2011 and 2016 and the percent conifer cover from the USFS EVeg. All pixels were screened to include only locations at 600 to 2300 m elevation and 35.69 to 37.65 ^{o} latitude, no reported fire since 1980, a 30-year Normal *P* of at least 600 mm yr^{-1} and a conifer dominated WHR class (e.g., only WHR SMC, PPN, MHC, LPN, RFR, WFR, SCN, JPN, DFR, EPN, PJN). Aspect was calculated from the DEM and pixels were binned and averaged at 10° intervals.
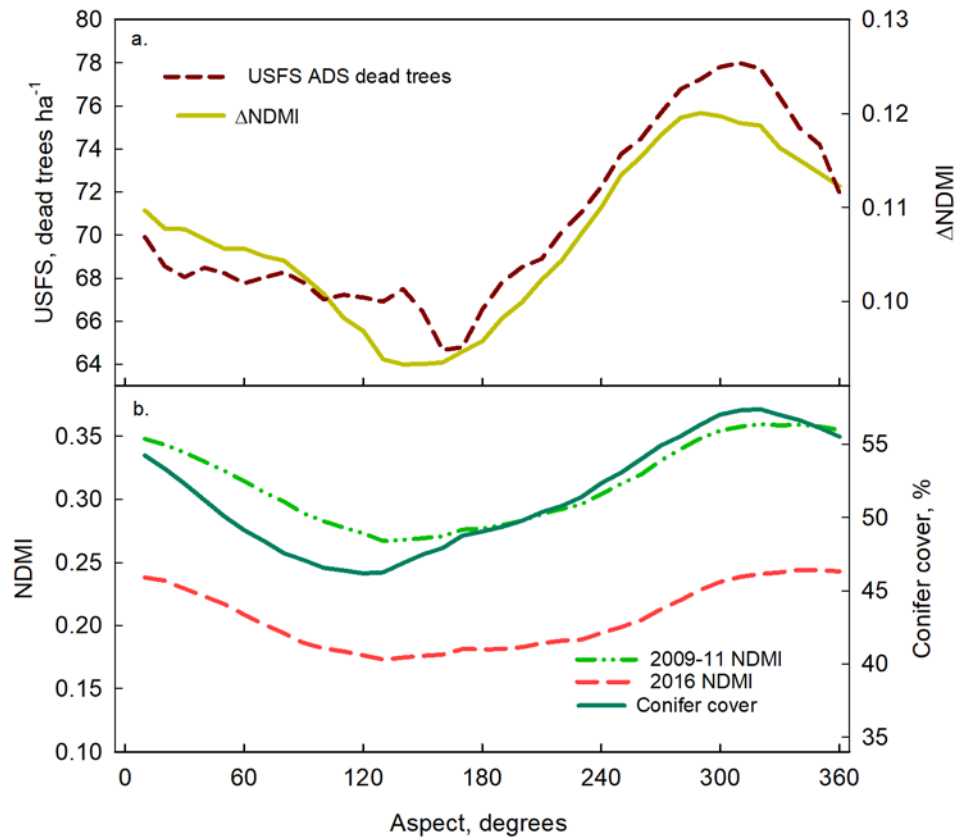
Figure S10: (a) Annual Water Year (Oct-Sept) cumulative Evapotranspiration (*ET*) in the southern Sierra Nevada calculated four ways: i. using the mean ET averaged across all pixels and all years (ET_{mean}); ii. considering only *NDVI* (Fig. S6) ($ET_{just\ NDVI}$); iii. considering only the normalized saturated vapor pressure calculated from Tmax ($ET_{just\ T}$); and iv. considering both vapor pressure and *NDVI* ($ET_{T\ and\ canopy}$). (b) Annual Water Year (Oct-Sept) cumulative Precipitation (*P*) in the southern Sierra Nevada, and *P-ET* calculated using ET_{mean} and $ET_{T\ and\ canopy}$).
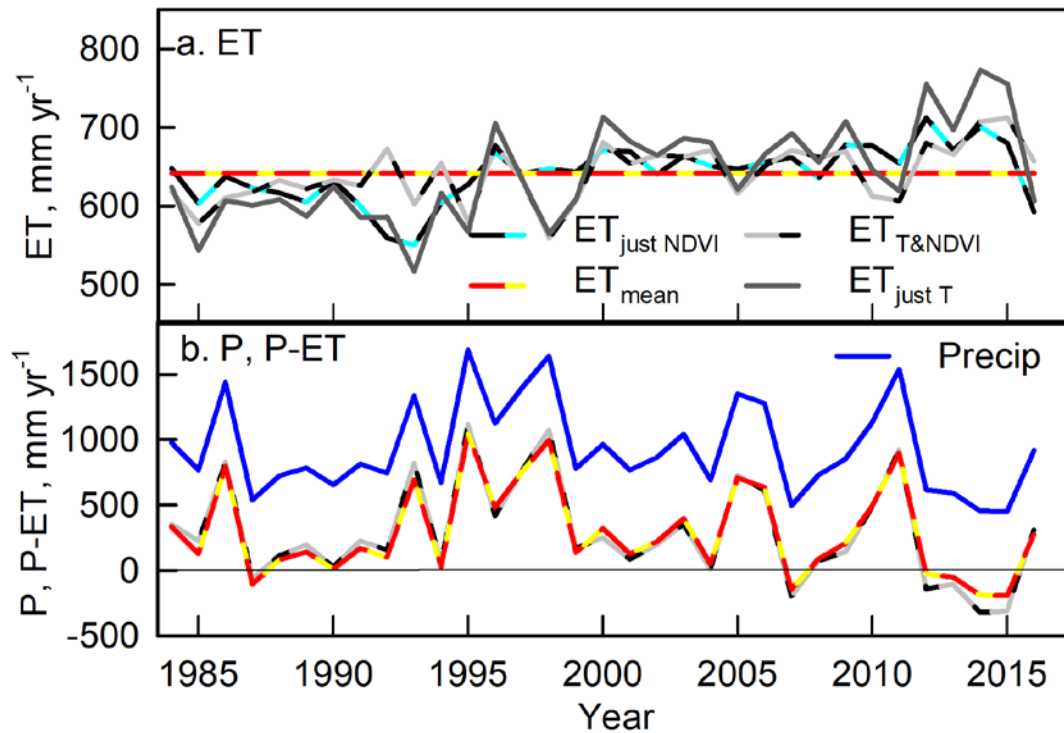
Figure S11: Conceptual model of the controls on tree mortality in the Sierra Nevada during the 2012-15 drought. Mortality was closely associated with an extreme *P-ET* overdraft (Fig. 1c, 2, 3, 4a, S1, S2bc, S8a). An extreme *P-ET* overdraft was associated with reduced *P* and drought, and also increased *ET* as mediated by warmer than usual air temperatures and antecedent canopy expansion (Fig. 4b,S5). Antecedent canopy expansion was associated with wetter and warmer periods (Fig. S10).
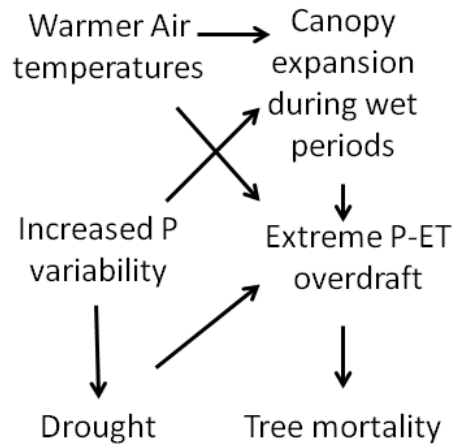
Figure S12: Comparison of (a) NDVI and (b) NDMI time series for each Landsat instrument after homogenization. Lines connect summer means for July to September. Pixels were screened for locations within 35.69 to 37.65 latitude, no reported fire since 1980, a 30-year Normal P of at least 600 mm yr^{-1} and a conifer dominated WHR class (e.g., only WHR types SMC, PPN, MHC, LPN, RFR, WFR, SCN, JPN, DFR, EPN, PJN).